Impact of ~~offshore and onshore~~ wind profiles on ~~ground generation~~ ground-generation airborne wind energy system performance

Markus Sommerfeld[1], Martin Dörenkämper[2], Jochem De Schutter[3], and Curran Crawford[1]

[1]Institute for Integrated Energy Systems, University of Victoria, British Columbia, Canada
[2]Fraunhofer Institute for Wind Energy Systems (IWES), Oldenburg, Germany
[3]Systems Control and Optimization Laboratory IMTEK, University of Freiburg, Germany

Correspondence: Markus Sommerfeld (msommerf@uvic.ca)

Abstract. ~~Airborne~~ This study investigates the performance of pumping mode ground-generation airborne wind energy systems(AWESs) ~~aim to operate at altitudes above conventional wind turbines (WTs) and harvest energy from stronger winds aloft. This study investigates these claims by determining dynamic,~~ by determining cyclical, feasible, power-optimal flight trajectories ~~, operating heights subject to realistic offshore and onshore wind conditions. The utilized wind speed profilesare based on simulated offshore and onshore 10-minute mesoscale wind conditions which are analyzed and categorized using k-means clustering~~based on realistic vertical wind velocity profiles. These 10-minute profiles, derived from mesoscale weather simulations at an offshore and an onshore site in Europe, are incorporated into an optimal control model that maximizes average cycle power by optimizing the trajectory. To reduce ~~computational cost of the trajectory optimization~~the computational cost, representative wind ~~speed profiles from each cluster are implemented into the `awebox` optimal control model to determine feasible, power-optimal trajectories~~conditions are determined based on k-means clustering. The results describe the influence of wind speed magnitude and profile shape on ~~optimal trajectories, tether speed, tether length and tension. Optimal operating heights are generally below 400 m with most AWES operating at around 200 m. This study compares power curve visualizations for a constant reference height of 100 m to an apriori operating altitude guess of 100 - 400 m to the pattern trajectory height. Power curves are estimated based on average cyclepower and compared to wind turbine (WT) and quasi-steady-state AWES reference model (QSM) performance. A power curve comparison between~~ the power, tether tension, tether reeling speed and kite trajectory during a pumping cycle. The effect of mesoscale-simulated wind ~~conditions and logarithmic wind speed profiles shows that the offshore location is reasonably well approximated by logarithmic wind speed profiles. Realistic wind data onshore often outperform the logarithmic reference due to the higher number of~~ profiles on power curves is illustrated by comparing them to logarithmic wind profiles. Offshore, the results are in good agreement, while onshore power curves differ due to more frequent non-monotonic wind ~~speed profiles .~~ conditions. Results are references against a simplified quasi-steady-state model and wind turbine model. This study investigates how power curves based on mesoscale-simulated wind profiles are affected by the choice of reference height. Our data shows that optimal operating heights are generally below 400 m with most AWESs operating at around 200 m.

1 Introduction

Airborne wind energy systems (AWESs) aspire to harvest stronger and less turbulent winds at mid-altitude, here defined as heights ~~above~~ between 100 ~~m and below~~ and 1000 m, presumably beyond what is achievable with conventional wind turbines (WTs). The prospects of higher energy yield combined with reduced capital cost motivate the development of this ~~novel~~ new class of renewable energy technology (Lunney et al., 2017; Fagiano and Milanese, 2012). Unlike conventional WTs, which ~~over the last~~ in recent decades have converged to a single concept with three blades and a conical tower, several different AWES concepts and designs are ~~still under investigation~~ being investigated by numerous companies and research institutes ~~(Cherubini et al., 2015)~~(Cherubini et al., 2015; **?**; **?**). These kite-inspired systems consist of three main components: one or more ~~flying wings~~ tethered aircraft or kites, one or more ground stations, and one or more tethers to connect ~~them~~the flying components to the ground. This study focuses on the two-phase ~~, ground generation~~ cyclic, ground-generation concept, also referred to as pumping mode (Luchsinger, 2013). During the reel-out ~~phase the wing~~ or production phase, the kite pulls a tether from a drum on the ground, which is connected to a generator, thereby producing electricity. This is ~~then~~ followed by the reel-in phase during which the ~~wing adjusts its angle of attack to reduce aerodynamic forces and returns to its initial position~~kite returns to its initial position and reduces its aerodynamic forces in order to de-power. There are several ways to reduce the aerodynamic forces on a kite, such as adjusting its angle of attack or flying it out of the wind window. Various other concepts such as fly-gen, aerostat, or rotary lift are not considered in this study (Cherubini et al., 2015).

Since this technology is still ~~at an~~ in a relatively early stage of development, validation and comparison of ~~results~~ power production estimates is difficult. ~~A~~ Several studies (**?**Schelbergen et al., 2020; **?**; Ranneberg et al., 2018) compared computed power curves with experimental performance data. At present, there is no standardized power curve definition ~~and reference design , similar to Jonkman et al. (2009) or Gaertner et al. (2020), will enable~~ or reference design that would allow for comparison between different concepts and ~~to~~ conventional wind turbines. However, the goal of **?**Eijkelhof et al. (2020) was to create a reference design for a multi-MW AWES. It is not the goal of this study to determine ~~such~~ a general power curve, but rather ~~investigate the variation in power stemming~~ to investigate the power variation of a specific design derived from realistic wind profiles.

Recent consensus among the scientific community defined a power curve as the maximum average cycle ~~trajectory powerover~~ power, which is the combination of a consecutive reel-out and reel-in phases, as a function of wind speed at pattern ~~trajectory~~ height, which is the ~~expected or actual~~ time-averaged height during the reel-out ~~(power production)~~ power-producing phase (Airborne Wind Europe, 2021). Together with the site-specific wind resource, ~~power curves help~~ wind park planners and manufacturers can use power curves to estimate annual energy production (AEP), ~~Levelized cost~~ which can be combined with a cost model to determine the levelized cost of electricity (LCOE) and ~~determine~~ financial viability (Malz et al., 2020a). ~~The glossary does not yet define an estimation method for these metrics. In contrast to conventional WT~~Unlike conventional WTs, where the wind speed probability distribution at hub height is used to determine AEP, AWES continuously change their operating height, making it difficult to determine AEP with this approach. ~~Furthermore, the performance of AWESs is highly dependent~~ AWES performance highly dependents on the shape and magnitude of the wind speed profile over ~~a~~

rangealtitudes. Simple the operating height range. Using simple wind profile approximationsusing , such as logarithmic or exponential wind speed profiles, which are often erroneously applied beyond earth's surface layer (Optis et al., 2016), might approximate can provide an estimate of long-term average conditions, but cannot capture the broad variation . However, these approximations cannot account for the wide range of profile shapes that exist on short timescales (Emeis, 2013). They are therefore an inappropriate approximation of instantaneous wind conditions and do not capture diurnal or seasonal changes , which can lead to power outputvariationoccur over short periods of time or changes that occur on a daily or seasonal basis (Emeis, 2013). This can reduce the accuracy of the predicted power output. However, they such wind speed profiles can be employed to estimate average performance and are the standard in most AWES power estimation studies. An early performance analysis by Heilmann and Houle (2013) used

In their study, **?** described TU Delft's 20 kW inflatable wing technology demonstrator and compared a statistically derived power curve to results from a theoretical performance model. The wind and power models used in this study were taken from **?**. The wind model is based on a standard exponential wind speed profiles with a wind shear exponent of 0.15 profile approximation, while the power model uses a multi-phase QSM. A follow up study (van der Vlugt et al., 2019), added more detail to specific cycle trajectories. Heilmann and Houle (2013) used exponential wind speed profiles and a standard Rayleigh distribution with 7 ms^{-1} to estimate performance and cost. Ranneberg et al. (2018) describes Their power curve is modeled based on a QSM by Luchsinger (2013) using the averaged flight path height of the kite as wind speed reference height. An LCOE between 40 and 110 Euro/MWh was estimated for different annual average wind speeds. Faggiani and Schmehl (2018) used a similar pumping-mode QSM to estimate power output based on wind speed at the operating height of the kite. They developed a cost model to estimate the achievable LCOE of an entire kite wind farm. Their analyses showed that the cost of energy decreases and the quality of the electrical power increases with increasing number of kites. Ranneberg et al. (2018) studied the performance of a soft kite pumping mode AWES with a family of by determining its power curves at different fixed altitudes, which correspond to the findings in this researchvarious reference heights for different logarithmic wind profiles. The study found that the yield variation for these logarithmic wind profiles was quite small. Additionally, the yield for a specific site was estimated using detailed wind speed profiles from COSMO-DE and the results were found to be consistent with more detailed simulations of the Enerk'ite EK30 prototype (noa, 2016). Leuthold et al. (2018) investigated power-optimal trajectories and performance of a ground generation multi kite of a ground-generation multikite configuration for a range of logarithmic wind speed profiles. Three distinct operational regions were identified: Region I where power is used to maintain altitude, Region II where power harvesting increases up to design wind speed, and Region III where power extraction is intentionally limited due to the physical constraints of the system. Licitra et al. (2019) estimated the performance and power curve of a ground generation, fixed-wing fixed-kite ground-generation AWES by generating power-optimal trajectories and validating them against Ampyx using a power law approximation of the wind speed profile. The results were validated against data from Ampyx Power AP2 data (Licitra, 2018; Malz et al., 2019; Ampyx, 2020), which is also used in this research. The optimal, single-loop trajectory was defined by a simple power law approximation of the wind speed profile. Because of the the upscaling drawbacks of . **?** found that mass had a detrimental effect on power-optimal trajectories for large-scale single-kite AWES, fixed-wing AWES. To determine power curves, the authors used normalized

average offshore wind speed profiles from the Ijmuiden measurement tower. **?** used the same methodology and wind data as in this study to examine the effects of size scaling and improvements in aerodynamic efficiency on a single-kite fixed-wing reference system. The authors found that it is likely better to deploy multiple smaller-scale devices rather than a single large-scale system, because of negative mass scaling effects. De Schutter et al. (2019) analyzed the performance of utility scale, stacked ~~multi-kite systems , using the same optimization framework as this research. Onshore and offshore~~ multikite systems using logarithmic wind speed profiles ~~serve~~ as boundary conditions for ~~the non-linear~~ a nonlinear optimization problem. ~~Malz et al. (2020b) optimized performance, based on the model described in (Malz et al., 2019), for clustered wind speed profiles, similar to this research. To reduce computation time, wind data~~ The authors used the same optimization framework as in the present investigation. They found that this multikite strategy could make power generation largely independent wing size. Malz et al. (2020b) efficiently estimated the performance of single-kite drag-mode AWES for large wind data sets by combining an optimal control performance model with smart initialization and machine learning. Wind speed profiles from the MERRA-2 reanalysis model (**?**) were clustered into characteristic profile shapes and ~~sorted by average wind speed . This allowed for the initial guesses of every subsequent optimization to be based on the previous results~~interpolated using Lagrangian polynomials (Section 4.4). The authors showed that ordering the wind parameters by the wind speed at the average operational height (300 m) significantly reduced the computation time. Aull et al. (2020) explored the design and sizing of fly-gen ~~rigid-wing~~ rigid-kite systems based on a steady-state model with simple aerodynamic and mass-scaling approximations. At each scale, the relationships between size, efficiency, power output, and cost were determined. The wind resource was described by an exponential wind shear model with a Weibull distribution. ~~Bechtle et al. (2019) The authors describe the potential energy yield without accounting for a specific power conversion mechanism . The investigation includes~~ wind resources at high altitudes throughout Europe. They described the available wind energy without considering a specific conversion mechanism and included a description of wind speed and probability ~~for several heights. Schelbergen et al. (2020) compares energy production based on this data set to performance based on~~ at various heights. The effect of variable height harvesting was demonstrated for a location in the English Channel. Schelbergen et al. (2020) proposed a clustering procedure to obtain wind statistics from the Dutch Offshore Wind Atlas (DOWA) ~~and light detection and ranging (LiDAR) data . The authors used principal~~ data set. Principal component analysis and ~~*k*-means clustering~~ k-means clustering were used to determine representative wind speed ~~profiles for a part~~ profile shapes. To estimate the AEP of a small-scale pumping AWES located at Cabauw in the center of the Netherlands~~and the North Sea. They derived power curves and estimated AEP from wind statistics for several locations. Faggiani and Schmehl (2018) investigated aspects of joint operation, such as spacial stacking of the systems,~~ several power curves were derived for each wind speed profile shape using a flexible-kite, pumping mode QSM developed by van der Vlugt et al. (2019). Faggiani and Schmehl (2018) studied the economic impact of various design aspects of wind parks, including the spatial stacking of systems, the number of units, the size of kites, and phase-shifted operation~~of several 100 kW soft wing pumping kite systems arranged in a wind park. Performance was estimated by a quasi-steady-state model (QSM) (Schmehl et al., 2013; van der Vlugt et al., 2019), similar to the one used for in this research, subject to a standard logarithmic wind profile.~~

~~Wind~~ . The performance of the system was estimated using a QSM developed by Schmehl et al. (2013); van der Vlugt et al. (2019) , assuming a range of wind speeds at the operating height of the kite. The AEP LCOE could be assessed by combining a detailed cost model with an assumed Weibull probability distribution. The study found that increasing the number of kites had several scale effects, such as decreasing the cost of energy and increasing the quality of electrical power. Wind speed profiles are governed by weather phenomena, environmental and location-dependent conditions ~~(e.g. surface roughness)~~ on a multitude of temporal and spatial scales. The preferred means of determining wind conditions for wind energy converters are long-term, ~~high resolution measurements, which at~~ high-resolution measurements. At mid-altitudes~~can solely be achieved by~~ , these measurements can only be obtained through long-range remote sensing methods such as LiDAR (light detection and ranging) or SoDAR (sonic detection and ranging). Measuring wind conditions at mid-altitudes is costly and difficult, due to reduced data availability (Sommerfeld et al., 2019a). Additionally, publicly available measurements are ~~hard to find because they are typically proprietary~~scarce. Therefore, wind data in this study ~~are exclusively based on~~ is derived from Weather Research and Forecasting model (WRF) mesoscale simulations (Skamarock et al., 2008)~~, but~~ . However, the described trajectory optimization methodology can be applied to any wind data set such as wind atlas data or measurements. Numerical mesoscale weather prediction models such as ~~the~~ WRF, which is well known for conventional WT siting applications (Salvação and Guedes Soares, 2018; Dörenkämper et al., 2020), are used to estimate wind conditions on time scales of a few minutes to years. Sommerfeld et al. (2019b) ~~compares~~ compared the simulated onshore data used in this study, located in northern Germany near the city of Pritzwalk, to LiDAR measurements and found a good ~~, but altitude-dependent~~ agreement between both data sets. ~~The simulated offshore conditions used in this study can be references against data at~~ Data from the FINO3 research platform in the North Sea ~~. This study investigates AWES performance~~ can be used as a reference for the simulated offshore conditions in this study. The present study investigates the performance of AWES subject to 10-minute average wind data, which is the standard for conventional WT, while the New European Wind Atlas (NEWA) only provides 30-minute average data (Witha et al., 2019). We use this ~~higher resolution~~ higher-resolution wind data because the higher temporal, spatial, and vertical resolution reduces averaging and allows for the investigation of more realistic wind conditions.

~~The key contribution of this paperis the investigation of power-optimal AWES performance subject to~~ This paper's main contribution is the examination of how realistic onshore and offshore wind profiles~~and its impact on average cycle power variation. Therefore, WRF-simulated wind data are used instead of assuming a wind profile relationship such as the logarithmic or exponential wind profile. Furthermore, this~~ , compared to a standard log profile, affect the power-optimal performance of AWES, and how the choice of reference height impacts the power curve, particularly given the wide range of wind speed profile shapes. This study is a continuation of previous analyses of LiDAR measurements (Sommerfeld et al., 2019a) and WRF simulations (Sommerfeld et al., 2019b) at the onshore ~~locatio. To justify the realism~~ location. To demonstrate the validity and applicability of the data~~location specific~~ , several wind characteristics are described. These include annual wind speed probability distributions up to 1000 m, annual wind direction statistics and wind speed profile shapes. The data are categorized using ~~*k*-means clustering which classifies each locations wind data~~ k-means clustering (Lloyd, 1982; **?**) which classifies the wind data at each location into groups of similar wind speed ~~magnitude and~~ and vertical profile shape. ~~From these clusters three representative profiles are sampled and implemented into the `awebox` optimization toolbox~~ Three representative 10-minute

wind velocity vectors $\mathbf{U}$ are sampled from each of these 20 clusters (total 60 vectors out of 52,560 wind data points per location) and serve as boundary conditions ~~. By selecting these profiles based on their average wind speed between 100 and 400 m, which is an apriori~~ for the `awebox` trajectory optimization (De Schutter et al., 2020). The profiles with the 5th, 50th, and 95th percentile of wind speed at an a priori guess of the pattern trajectory height ~~(Airborne Wind Europe, 2021), we use actual simulated data instead of averaged data. By choosing the 5th, 50th, 95th percentile, we~~ $z_{\text{pth}} \approx 100\ \text{m} \leq z \leq 400\ \text{m}$ (Airborne Wind Europe, 2021) are selected because they encompass the most ~~likely operating~~ probable wind conditions within each cluster ~~and avoid~~ while excluding non-representative ~~profile extrema.~~ extremes. Subsection 6.3 verifies that choice and compares the impact of reference height on the power curve. This drastically reduces the computational cost as only few selected profiles are ~~needed~~ used to represent the entire ~~wind spectrum . This study only uses 60 out of 52560 10-minute wind profiles. This is sufficient for the scope of this study, which includes the analysis of representative operating conditions and the estimation of powercurves~~spectrum with sufficient resolution to investigate the variation of power.

The `awebox` optimization model allows for the investigation of dynamic performance parameters, such as aircraft trajectories, tether tension, tether reeling speed and power which highly depend on the wind conditions. The aircraft model is based on the well investigated and published Ampyx Power AP2 prototype (Licitra, 2018; Malz et al., 2019; Ampyx, 2020), ~~scaled to a wing~~ adjusted to a projected surface area of $A = 20\ \text{m}^2$ ~~. The optimize~~ to generate results for more realistic and probable devices. The maximized power curves, estimated based on average cycle powers ~~are referenced against optimal performance subject to a simple logarithmic wind speed profile, a quasi-steady-state reference AWES model (QSM),~~ and wind speed at reference height $\overline{U}_{\text{ref}} = U(z_{\text{ref}})$, are compared to performance predictions using a simple AWES QSM and a steady-state WT ~~power estimation. The apriori guess of 100 and 400 meter reference height is verified by comparing AWESs power curvesover wind speed at reference height to wind speed at pattern trajectory height~~model. The variation in performance caused by realistic wind data is referenced against predictions based on simple logarithmic wind speed profiles. The a priori guess of $100\ \text{m} \leq z_{\text{ref}} \leq 400\ \text{m}$ is confirmed by comparing the impact of different reference heights on the power curves.

The ~~paper is structured as follows:~~ structure of this research is as follows. Section 2 introduces the mesoscale WRF model~~setup. Section 2.2 analyzes the onshore and offshore wind resource. Section 2.3 introduces the k-means~~ , analyzes the offshore and onshore wind resource, introduces the k-means clustering algorithm and summarizes ~~results of clustered wind profiles (both longitudinal and lateral wind components). For visualization purposes data are shown for k = 10 clusters, while 20 clusters are used in the later analysis.~~ the results of the clustered wind vectors. Section 3 introduces the dynamic AWES model, ~~comprising of aircraft , tether and ground-station models~~which includes an aircraft and tether model as well as ground station constraints. Section 4 describes the `awebox` optimization ~~framework~~toolbox, summarizes the aircraft parameters, system constraints, and initial conditions. This is followed by a description of the WT and AWES reference models in ~~section 5. Section 6 presents the results which~~ Section 5. The results presented in Section 6 include flight trajectories and time series ~~of~~ data for various performance parameters, as well as a statistical analysis of ~~tether length and operating altitudeas well as a power curve estimation. Finally, Section 7~~ the tether length, operating altitude, and power curve estimations. Section 7 summarizes the findings and concludes with an outlook and motivation for future work.

2 Wind conditions

~~As of now no universally accepted mid-altitude AWES reference wind model exists. Therefore we analyze~~ Subsection 2.1 introduces the model and setup of the onshore and offshore ~~wind conditions based on the mesoscale WRF model introduced in Sub-section 2.1. Sub-section 2.2 analyses~~ mesoscale WRF simulations. Subsection 2.2 analyzes wind statistics to ~~gives an instight~~ give an insight into the wind regime at both locations. Clustering, ~~introduced in Sub-sections~~ which is introduced in Subsection 2.3, is used to ~~determine~~ identify groups of similar ~~wind profiles from which unaveraged, representative profiles are sampled~~vertical wind profiles and to select representative profiles from these groups. This significantly reduces the computational cost as only few selected profiles are necessary to represent the wind regime~~and to approximate the power curves. Sub-sections~~ . Subsections 2.4 and 2.5 describe the resulting clusters and their statistical correlation with temporal and meteorological ~~phenomenon~~phenomena.

2.1 Mesoscale simulations

This study compares AWES performance for two specific onshore and offshore locations in Europe (Figure 1). Wind conditions for the chosen years are assumed to be representative of these locations. However, the wind data has not been compared to long-term wind atlas data and has not been corrected using long-term simulations. The onshore data ~~represents~~ represent wind conditions at the Pritzwalk Sommersberg airport (lat: $53°10'47.00''$N, long: $12°11'20.98''$E) in northern Germany and ~~comprises~~ comprise 12 months of WRF simulation data between September 2015 and September 2016. The area surrounding the airport ~~mostly consists~~ consists mainly of flat agricultural land with the town of Pritzwalk ~~to~~ in the south and is ~~therefore a fitting location for wind energy generation~~ a suitable location for the generation of wind energy (Sommerfeld et al., 2019a, b). The FINO3 research platform in the North Sea (lat: $55°11,7'$N, long: $7°9,5'$ E) was chosen as a representative offshore location due to ~~the~~ its proximity to several offshore wind farms and the amount of comprehensive reference measurements (Peña et al., 2015). The offshore simulation covers the time frame between September 2013 and September 2014.

The mesoscale simulations ~~use~~ used the Weather Research and Forecasting (WRF) model (Skamarock et al.). The onshore simulation was performed with version 3.6.1 (Skamarock et al., 2008) prior to the 2018 release of WRF version 4.0.2 (Skamarock et al., 2021)~~in which the~~ , in which offshore simulations were computed. The setup of the model ~~has been~~ was adapted and constantly ~~optimized~~ improved for wind energy applications by the authors of the present manuscript ~~with the framework of~~ within for various projects and applications in recent years (Dörenkämper et al., 2015, 2017; Dörenkämper et al., 2020; Hahmann et al., 2020; Sommerfeld et al., 2019b). The focus of this study is not on the detailed comparison between mesoscale models, but on AWES performance subject to realistic onshore and offshore wind conditions. Both WRF models provide adequate ~~wind data for~~ temporal and spatial resolution for preliminary performance assessment, even though the setup and time frame are different.

Each simulation consists of three nested domains around their respective location (black dot ~~) shown in Figure 1.~~ Figure 1). The innermost domain (D03), with the finest resolution, is nested within the middle domain (D02), which in turn is nested within the outermost domain (D01) with the coarsest resolution. The simulations use one-way nesting where the

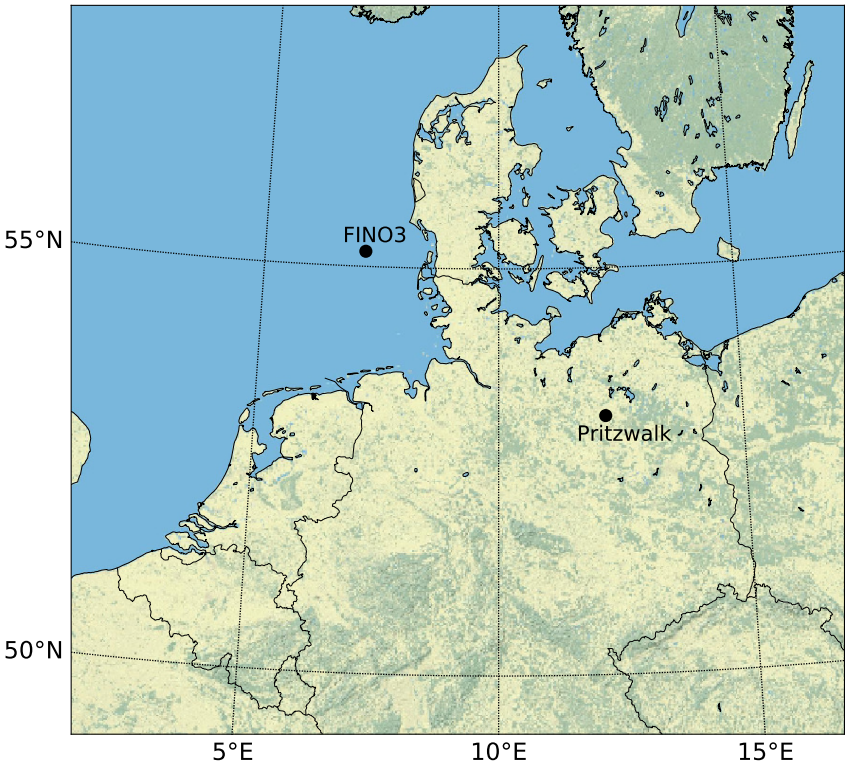

Figure 1. Map of northern Germany with the representative onshore (Pritzwalk) and offshore (FINO3) locations highlighted by black dots.

outer domains define the boundary conditions for the inner domains. Atmospheric boundary conditions are defined by ERA-Interim (Dee et al., 2011) for the onshore location and by ERA5 (Hersbach and Dick, 2016) reanalysis data for the offshore location, while sea surface parameters (such as sea surface temperature and sea ice analysis) for the offshore location are based on OSTIA (Donlon et al., 2012). These data sets have proven to provide good results for wind ~~energy relevant~~ energy-relevant heights and sites (Olauson, 2018; Hahmann et al., 2020). Four-dimensional data assimilation (FDDA), also known as analysis nudging, nudges the simulation of the outer domain towards the atmospheric boundary conditions throughout the simulation time, to reduce numerical drifting and provide smoother boundary conditions. Both simulations use the ~~MYNN~~ Mellor–Yamada–Nakanishi–Niino (MYNN) 2.5 (Nakanishi and Niino, 2009) level scheme for the planetary boundary layer (PBL) physics~~(Nakanishi and Niino, 2009). While the~~ . The onshore simulation was ~~performed~~ carried out in a single ~~12 month spanning simulation~~ 12-month simulation run from 2015-09-01 to 2016-08-31~~), the~~ . The offshore simulation period ~~consisted of~~ covered a 410 ~~days (~~day period from 2013-08-30 to 2014-10-14 ~~) that was split~~ and was divided into 41 simula-

tions of 10 days each, with an additional 24 hours of spin-up time per run. Spin-up ~~describes the period during~~ is the period in which the model produces ~~unreliable results due to the initialization based on a coarser ,~~ results that may not be reliable due to initialization using coarser global atmospheric reanalysis data~~set. ~~. WRF calculates the vertical coordinate using a hybrid hydrostatic pressure coordinate, which is a function of surface and atmospheric pressure (Skamarock et al., 2021). The data at ~~every~~ each vertical, terrain-following ~~,~~ pressure coordinate (sigma level) ~~are transformed to the~~ is converted to geometric heights using the ~~post-processing methodology described in~~ postprocessing methodology described by Dörenkämper et al. (2020). Table 1 summarizes the key ~~parameters of the~~ model settings used in this study. All simulations were ~~run~~ performed on the *EDDY* High-Performance Computing clusters at the University of Oldenburg (Carl von Ossietzky Universität Oldenburg, 2018).

Table 1. Key setup parameters of the onshore and offshore mesoscale WRF simulations ~~Skamarock et al. (2008)~~to generate the wind data used in this study.

Model Parameter	Settings	
	Onshore	Offshore
WRF model version	3.5.1	4.0.2
Time period	2015-09-01 to 2016-08-31	2013-08-30 to 2014-10-14
Reanalysis data set	ERA-Interim	ERA5 & OSTIA
Horizontal grid size (D01, D02, D03)	120 ×120, 121 ×121, 121 ×121	150 ×150, 151 ×151, 151 ×151
Horizontal Resolution (D01, D02, D03)	27 km, 9 km, 3 km	18 km, 6 km, 2 km
Vertical grid levels	60 sigma levels (about 25 below 2 km)	60 sigma levels (about 25 below 2 km)
Nesting	one-way	one-way
Initialisation strategy	single run	240 h runs plus 24 h spin-up time
Nudging	Analysis nudging (FDDA)	Analysis nudging (FDDA)
PBL scheme	MYNN level 2.5	MYNN level 2.5

2.2 Wind regime

Figure 2 depicts the wind roses of the computed annual wind conditions at 100 m (a, b) and 500 m (c, d) height onshore (left) and offshore (right). The dominant wind direction at both locations is southwest, turning clockwise with increasing altitude.

Directional variability decreases and ~~wind speed~~ the wind speed U, which is the magnitude of the wind vector $\mathbf{U}$ increases with height, following the expected trends in the northern hemisphere (Arya and Holton, 2001; Stull, 1988). The average onshore wind direction turns about 14° between 100 and 500 m, whereas average offshore wind direction only veers approximately 5°. The offshore wind direction turns approximately 10° additional degrees above 500 m, resulting in roughly the same westerly wind direction at ~~high altitudes at~~ around 1000 m. Due to the prevailing unstable conditions offshore ~~, which~~

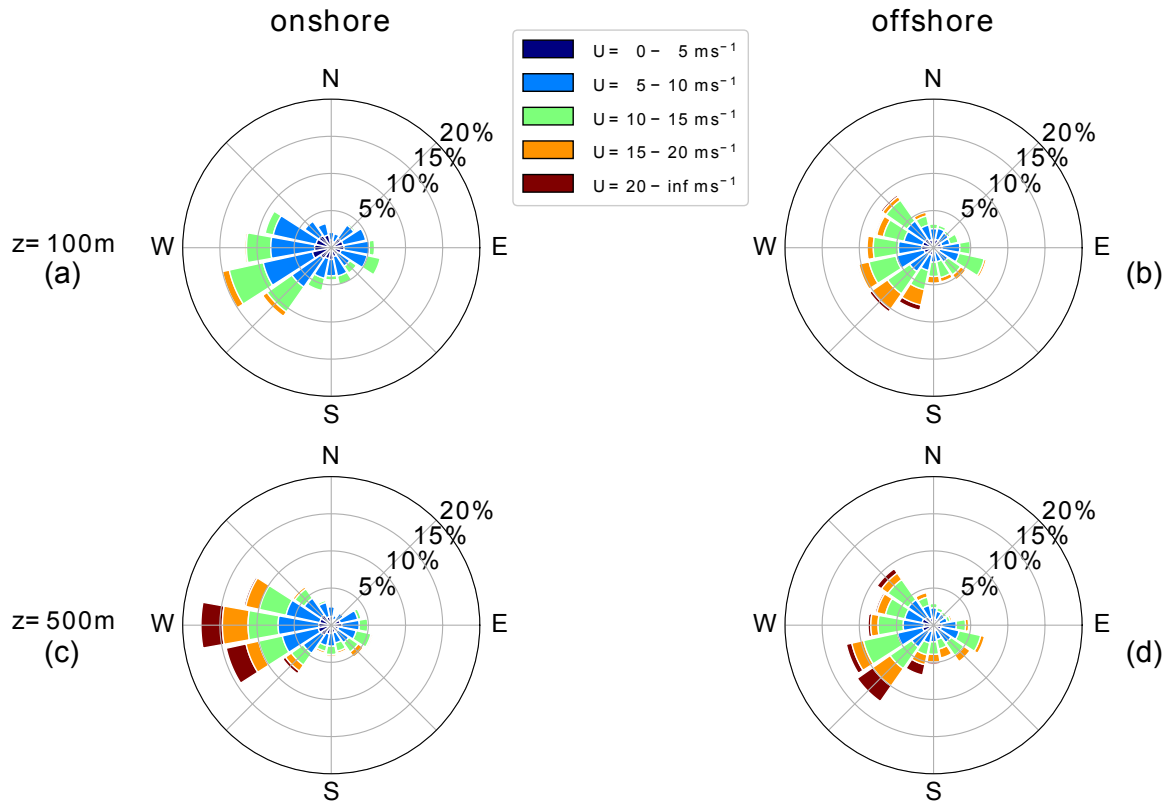

Figure 2. Wind roses of annual wind direction and speed statistics at Pritzwalk (onshore) and FINO3 (offshore) for heights of 100 and 500 m during the simulated ~~year~~years.

~~are~~ accompanied by strong vertical mixing, the investigated heights show less veer than onshore. ~~The wind~~ Wind shear at the offshore location is lower compared to the onshore location due to lower surface roughness.

Figure 3 shows the annual horizontal wind speed probability distributions at each height level for both locations. These distributions give ~~an~~ insight into the wind ~~speed~~ statistics at specific heights, but not into the statistics of the wind profile shapes. The ~~chosen~~ nonlinear color gradient allows for the representation of the entire relative probability range. Onshore (a) ~~wind speeds~~ U are relatively low and have a fairly narrow deviation below 300 m, due to dominant surface effects. Above this height the distribution broadens, but a high probability of low wind speeds remains for the ~~full~~ entire height range. The distributions show bimodal characteristics caused by different atmospheric stratification. Low wind speeds are commonly associated with unstable and high wind speeds with neutral or stable atmospheric conditions.

Such multimodal distributions at higher altitudes are better described by the sum of two or more probability distributions, as standard Weibull or Rayleigh distributions cannot capture this phenomenon (Sommerfeld et al., 2019a). Offshore U (b) ~~wind speeds~~ display a wider distribution at all heights as they are less affected by surface effects. ~~Similar~~ Similarly to onshore, the offshore frequency distribution also shows a high probability of lower ~~wind speeds~~ U (between 5-10 ms^{-1}) at all heights.

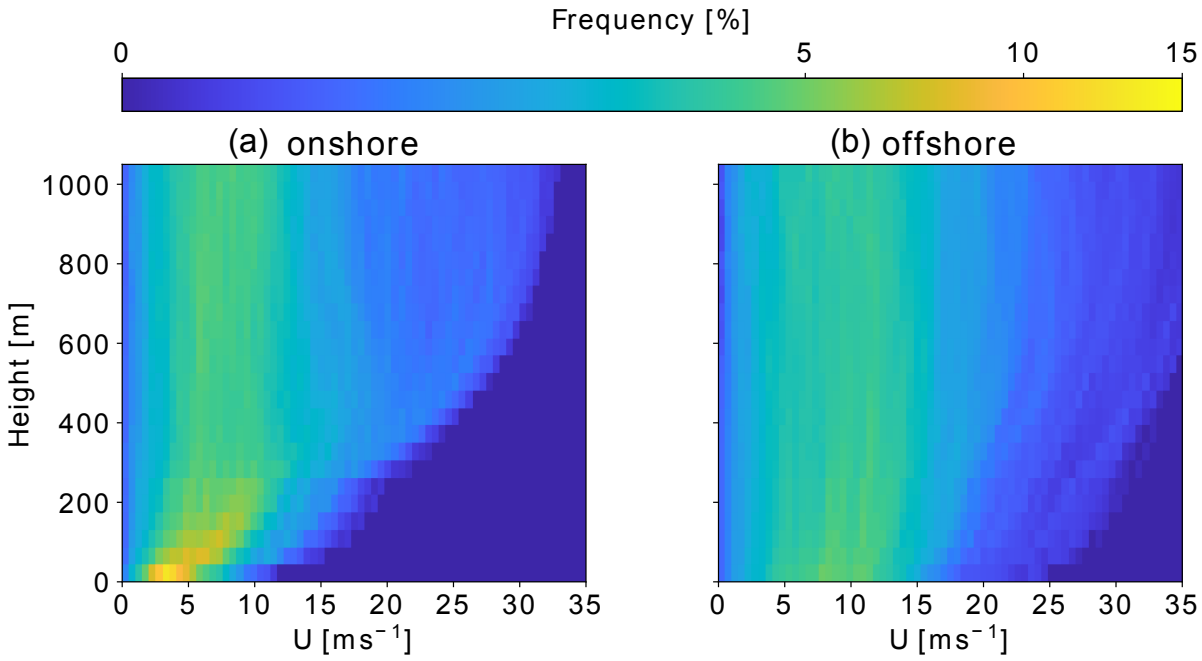

Figure 3. Comparison of WRF-simulated annual wind speed U probability ~~distribution~~ distributions at each height level between ~~Pritzwalk (~~onshore ~~left~~(a) and ~~FINO3 (~~offshore ~~right~~(b) up to 1000 m. ~~A~~ The nonlinear color scheme ~~is chosen to represent~~ represents the high probability of low altitude, particularly onshore~~winds ,~~ while still differentiating the lower, wide spread frequencies at higher altitudes.

Higher ~~wind speeds~~ U at lower altitudes ~~benefits~~ benefit conventional WT and weakens the argument for offshore AWES, as one of their benefits would be to harness energy from the stronger winds at higher altitudes. ~~Additional~~ However, other reasons for placing AWES offshore are the safety and land use regulations and the potential cost benefits of a smaller support structure (offshorewind.biz, 2018; Lunney et al., 2017; Ellis and Ferraro, 2016).

~~Atmospheric stability of the boundary layer~~The Obukhov length $\mathcal{L}$ (Obukhov, 1971; Sempreviva and Gryning, 1996)

$$\mathcal{L} = \frac{-u_*^3 \theta_\mathrm{v}}{kg} \left(\frac{1}{Q_\mathrm{S}} + \frac{0.61}{Q_\mathrm{L} \theta} \right), \tag{1}$$

commonly characterizes the near-surface atmospheric stability, which highly affects the shape of the wind speed profile ~~shape, is commonly characterized using the Obukhov length $\mathcal{L}$ (Obukhov, 1971; Sempreviva and Gryning, 1996). Here the application is extended~~ U, which is the magnitude of the wind velocity profile $\mathbf{U}$. We extent the concept to mid-altitudes ~~. $\mathcal{L}$ is defined by~~ between 100 and 1000 m. The Obukhov length is a function of u_* is the simulated friction velocity~~u_*,~~ θ_v the virtual potential temperature~~θ_v, potential temperature θ,~~ θ the potential temperature, Q_S the kinematic virtual sensible surface heat flux~~Q_S,~~ Q_L the kinematic virtual latent heat flux~~Q_L,~~ k the von Kármán constant ~~k and gravitational acceleration~~ and g ~~:~~

$$\mathcal{L} = \left(\frac{-u_*^3 \theta_\mathrm{v}}{kg}\right)\left(\frac{1}{Q_\mathrm{S}} + \frac{0.61}{Q_\mathrm{L}\theta}\right).$$

~~Various stability classifications using Obukhov length are defined~~ the gravitational acceleration. Various stability classifications based on the Obukhov length have been defined for different wind energy sites. Table 2 summarizes the Obukhov length bin widths ~~(Floors et al., 2011)~~ used by Floors et al. (2011) and the frequency of occurrence of each stability class onshore and offshore, consistent with Sommerfeld et al. (2019b).

Neutral stratification occurs approximately 20% of the year at both locations. The lower heat capacity of the land surface leads to a faster heat transfer and a quicker surface cool-off which favors the development of stable stratification (≈17% onshore vs ≈6% offshore). The offshore location has a higher probability of unstable conditions, which is likely caused by a warmer ocean surface compared to the air above (Archer et al., 2016).

Table 2. Stability classes based on Obukhov ~~lengths (Floors et al., 2011)~~ length $\mathcal{L}$ (bins from Floors et al. (2011)) and associated annual probability at Pritzwalk (onshore~~; 01.09.2015 - 31.08.2016~~) and FINO3 (offshore~~; 30.08.2013 - 14.10.2014~~), based on WRF ~~results~~simulations.

Stability class	$\mathcal{L}$ [m]	onshore	offshore
Unstable (U)	$-200 \leq \mathcal{L} \leq -100$	7.27%	13.66%
Nearly unstable (NU)	$-500 \leq \mathcal{L} \leq -200$	7.09%	16.34%
Neutral (N)	$\lvert\mathcal{L}\rvert \geq 500$	20.71%	22.82%
Nearly stable (NS)	$200 \leq \mathcal{L} \leq 500$	12.56%	5.15%
Stable (S)	$50 \leq \mathcal{L} \leq 200$	17.24%	6.20%
Very stable (VS)	$10 \leq \mathcal{L} \leq 50$	10.04%	2.96%
Other	$-100 \leq \mathcal{L} \leq 10$	25.09%	32.87%

Both unstable and stable conditions can lead to non-logarithmic and non-monotonic ~~wind speed~~ U profiles. Unstable conditions are often accompanied by almost uniform ~~wind speed~~ U profiles due to increased mixing, whereas low-level jets (LLJs) can develop during the nocturnal stable onshore boundary layer (Banta, 2008). Both locations have a high chance of unassigned conditions (labeled as "Other") which are mostly associated with low wind speeds. ~~All of which affect AWES operation conditions and power production.~~

2.3 Clustering of wind conditions

An accepted ~~methodology~~ method to describe the near-surface atmosphere is atmospheric stability, commonly quantified by the Obukhov length ~~(Obukhov, 1971; Sempreviva and Gryning, 1996)~~ (Obukhov, 1971; Sempreviva and Gryning, 1996), which exclusively uses surface data (Section 2.2 and Equation (1)). Previous studies (Sommerfeld et al., 2019a, b) showed that Obukhov-length-classified wind speed profiles U diverge with height, especially during neutral and stable conditions, which indicates vertically heterogeneous atmospheric stability and suggests that surface-based stability categorization is insuf-

ficient for higher altitudes. ~~Clustering wind velocity profiles based on their similarity results in more cohesive profile groups (Schelbergen et al., 2020). In contrast to classifying the wind regime~~ Unlike classifying wind regimes by atmospheric stability, which requires additional temperature and heat flux data, clustering only uses wind data at multiple heights ~~and groups~~ to group profiles by similarity. This results in more cohesive profile groups (Schelbergen et al., 2020). Therefore, clustering can also be applied to wind-only measurements such as LiDAR.

The ~~k-means~~ k-means clustering algorithm (Pedregosa et al., 2011) used in this study is chosen for its ease of use and scalability, due to the high dimensionality of the data set. Many other algorithms produce similar results, but a comparison between clustering algorithms is beyond the scope of this research. ~~Before clustering, the two horizontal wind velocity components u and v, whose vertical variation define the wind velocity profile,~~ The wind velocity profiles $\mathbf{U}'$ (Figure 4, black) are rotated such that the main wind component ~~(average wind direction between 100 m and 400 m) u_{main}~~ $\overline{U}(z_{\mathrm{ref}}) = \overline{U}(100\ \mathrm{m} \leq z \leq 400\ \mathrm{m})$ points in the positive x direction ~~and the transverse component u_{dev} is perpendicular to it, pointing in the positive y direction . This removes the directional dependency of the wind velocity profiles,~~ $\mathbf{U}$ (blue), in order to remove directional dependencies. The velocity components at each height level are decomposed into u in the main wind direction and into v perpendicular to it (red). The wind speed profile U is not shown. This results in more homogeneous clusters, and simplifies the comparison of wind data and `awebox` results. It is analogous to assuming omnidirectional operation. ~~The trajectory optimization still needs to adjust to changes in wind conditions with height.~~

The wind velocity data ~~set~~ up to 1000 m comprises of data points at 30 height levels and in 2 directions. The clustering algorithm assigns each data point to one of ~~k~~ the k clusters represented by their respective cluster mean, also called ~~"centroid"~~ the centroid. These centroids are chosen such that they minimize the sum of the Euclidean distances to every data point within each cluster. This cost function is also referred to as ~~"inertia " or "~~ inertia or within-cluster sum-of-squares~~"~~. As such, the centroids are usually not actual data points, but rather the clusters' average, and will at best coincide with a data point by chance. The ~~resulting cluster label is~~ cluster labels are the result of random initialization and ~~does not have any~~ has no mathematical meaning. We therefore sort and label the clusters by average ~~wind speed~~ $\overline{U}(z_{\mathrm{ref}})$ between 100 m - 400 m for the following analyses in ~~Sub-section~~ Subsection 2.4. The variable ~~k~~ k refers to the fixed ~~,~~ and predefined number of clusters. The choice of ~~k~~ k significantly affects the accuracy of the wind resource description, as well as the computational cost. The choice of ~~k~~ k is informed by the elbow method, named after the characteristic line chart ~~which~~ that resembles an arm, and the silhouette score. The ~~"elbow" "~~ elbow" (the point of inflection ~~on~~ of the curve) is a good indication that the underlying model fits well for the corresponding number of clusters. ~~k~~ k can be chosen at a point where the inertia reduction becomes marginally small or decreases linearly (Pedregosa et al., 2011).

Absolute values of inertia (Figure 5 (a)) are not a normalized metric and ~~therefore scales with~~ scale with the size of the considered data set. ~~The silhouette coefficients on~~ On the other hand, the silhouette coefficients (Figure 5 (b, d)) are normalized between -1 (worst) and 1 (best). They indicate the membership of a data point to its cluster in comparison to other clusters, i.e. the proximity of each data point in one cluster to data points in neighboring clusters (Pedregosa et al., 2011). A negative value suggests that a data point ~~is~~ could be assigned to the wrong cluster. The silhouette score, depicted by a dashed red vertical line, is the average of all silhouette coefficients for a fixed number of clusters ~~k.~~

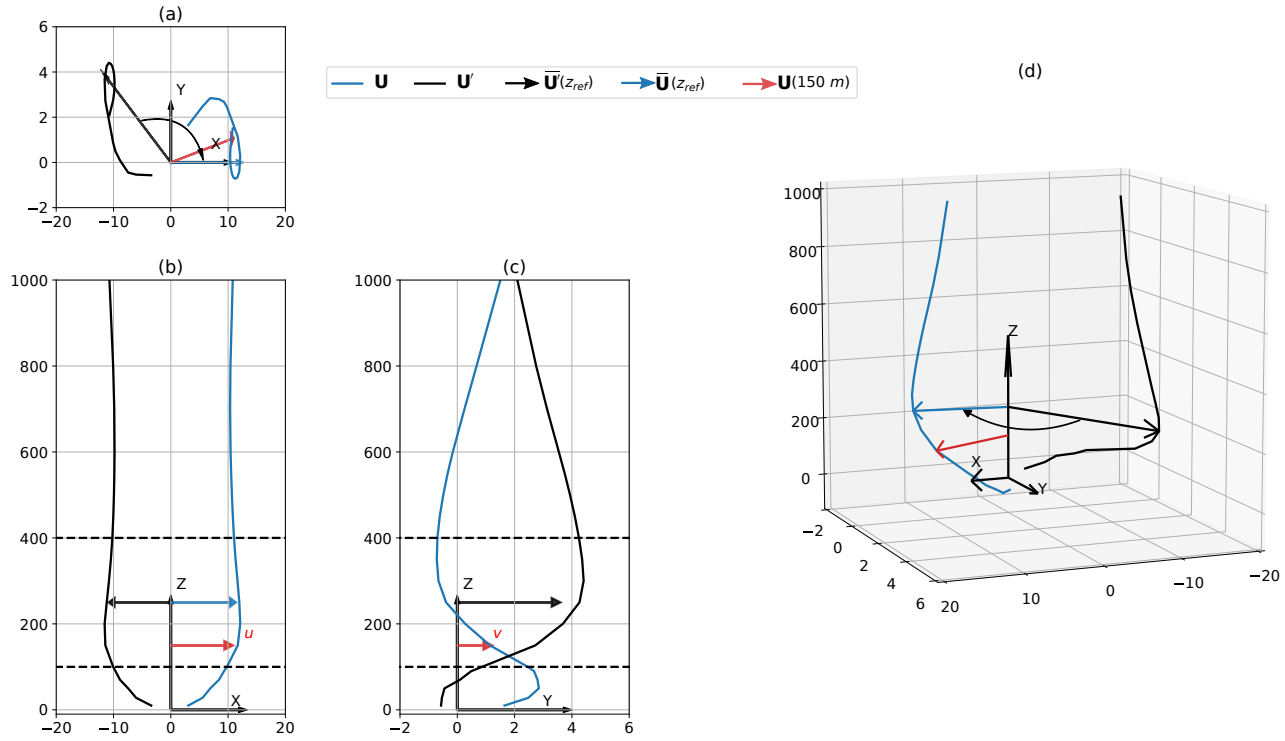

Figure 4. Representative wind velocity profile $\mathbf{U}'$ in its original direction and rotated so that the primary wind direction of the resulting profile $\mathbf{U}$ points in the x direction. Panel (a) shows the top view, panel (b) shows the front view, panel (c) shows the side view and panel (d) shows the isometric view. The primary wind direction is defined by the average wind vectors $\overline{\mathbf{U}}'(\mathbf{z}_{\text{ref}})$ (black) and $\overline{U}(z_{\text{ref}})$ (blue) between 100 and 400 m (dashed lines). As an example, the wind vector at $z = 150$ m (red) decomposed into u and v.

~~Figure 5 (a) shows the inertia (within-cluster sum-of-squares) for both locations. Figures 5 (b) and 5 (d) show the silhouette coefficients for every cluster for k~~ k. For visualization purposes, k=10 ~~, which is chosenhere for visualization purposes. The corresponding average silhouette score is depicted by a dashed, red, vertical line.~~ clusters have been chosen. Each cluster is sorted ~~by average wind speed~~ and color coded according to average $\overline{U}(z_{\text{ref}})$ between 100 m and 400 m and color~~coded corresponding to centroid average wind speed~~, same as Figure 6. Performing ~~this silhouette score analysis for multiple k~~ these silhouette score analyses for multiple k results in the trend shown in Figure 5 (c). A ~~k~~ k value of 20 seems to be a ~~decent~~ good choice for the available data sets~~as inertia only decreases moderately for~~ . This is because the decrease in inertia for a higher number of clusters ~~which does not justify~~ is only moderate, suggesting that the additional computational cost may not be worthwhile. Similarly, the silhouette score remains almost constant for higher numbers of clusters. Therefore, ~~k~~ k = 20 has been chosen for ~~later~~ the analyses in Section 6.

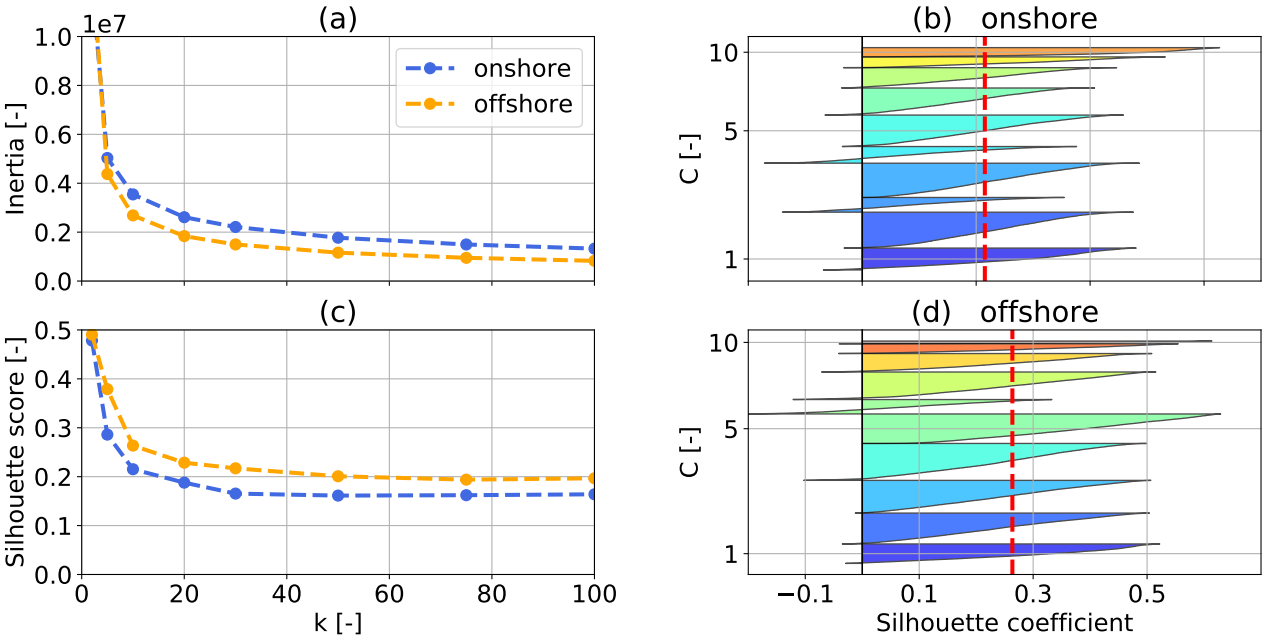

Figure 5.

~~*k*-means~~ k-means clustering inertia over of number of clusters ~~*k*~~ k (a) for one year of onshore (blue) and offshore (orange) wind velocity profiles U up to 1000 m. The ~~Onshore~~ onshore (b) and offshore (d) silhouette coefficients express the distance to neighbouring clusters and are color coded according to average ~~wind speed~~ $\overline{U}(z_{\mathrm{ref}})$ between 100 and 400 m, same as in Figures 6 9, 10 and 11. The red dashed line represents the silhouette score, which is the average silhouette coefficient. Silhouette score (c) over number number of cluster ~~*k*~~ k for both locations. The number of clusters ~~*k*~~ k = 10 has been chosen for presentation purposes only. ~~Later analyses use *k*~~ The analyses in the results section use k = 20 clusters.

2.4 ~~Analysis~~ Analyses of clustered profiles

For visualization purposes, the following ~~Sub-sections~~ subsections describe the wind conditions at both locations using only ~~*k*~~ k = 10 clusters. ~~Later analyses use *k*~~ The analyses in the results section (Section 6) use k = 20 clusters.

Figures 6 (a) and 6 (b) show the average ~~profiles~~ of the clustered wind ~~velocity profiles~~ speed profiles U, also referred to as centroids. Their ~~color~~ colors corresponds to the average ~~wind speed between~~ $\overline{U}(z_{\mathrm{ref}})$ between heights of 100 and 400 m. All WRF-simulated ~~wind speed profiles~~ U are depicted in gray. ~~Clusters~~ The cluster probabilities (Figures 6 (c, d)) are sorted by average centroid speed ~~between 100 and 400 m~~within the considered height range, represented by their colors and labels ($C = 1 - 10$).

As expected, offshore U (Figure 6 ~~b) low altitude wind speeds~~ (b)) at low-altitudes are higher and wind shear is lower than onshore (~~Figure 6 a). Overall~~Figure 6 (a)). In general, offshore centroids are ~~wider spread in comparison to the onshore profiles~~

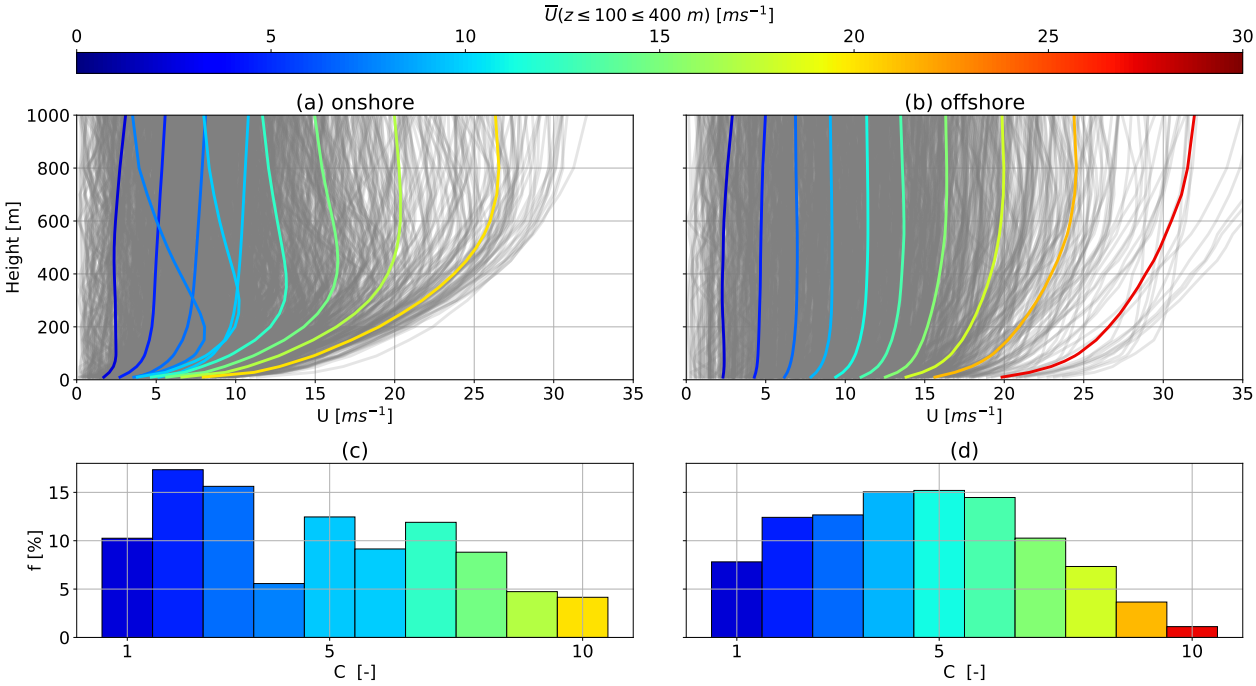

Figure 6. Onshore (left) and offshore (right) average annual wind speed profiles (centroids) resulting from ~~*k*-means~~ k-means clustering for ~~*k*~~ k = 10 (a,b). All comprising WRF-simulated wind speed profiles U are depicted in gray. The centroids are sorted, labeled and color coded in ascending order of average ~~wind speed~~ $\overline{U}(z_{\mathrm{ref}})$ between heights of 100 and 400 m. The corresponding cluster frequency of occurrence ~~*f*~~ f for each cluster ~~*C*~~ C is shown in (c) and (d) below.

~~and do not show a wind speed reversal. This indicates more homogeneous wind conditions offshore and a higher likelihood of LLJs onshore.~~ more monotonic, as they do not exhibit a distinct U peak (i.e. LLJs), and achieve higher maximum wind speeds than onshore. The U profiles within each cluster cover a relatively small range, suggesting consistent clusters. Figure 7 (onshore) and Figure 8 show the distribution of U within each of the clusters. At both locations, the first two clusters (Figures 7 (a, b) and 8 (a, b)) exhibit very low wind shear with ~~an almost constant wind speed~~ a low and almost constant U above 200 m. These low wind speed clusters amount to approximately 25 % onshore Figure 6 (c) and 20% offshore Figure 6 (d), as can be seen in the corresponding cluster frequency of occurrence ~~*f*~~f. A standard logarithmic wind profile does not accurately describe such almost constant profiles which could lead to an overestimation of ~~wind speeds~~ U at higher altitudes. ~~Therefore, AWESs need to be able to either operate under such low wind speeds or need~~ AWESs must either be capable of functioning at low U or be able to safely land and ~~take-off~~take off autonomously. Onshore clusters 4 and 5 (Figures 7 (d, e) and 8 (d, e)) seem to mostly ~~comprise~~ consist of non-monotonic profiles as these centroids show a distinct LLJ nose at about 200 m and 300 m. ~~Onshore~~ The offshore centroids of clusters 7 and 8 (Figures 7 (g, h) and 8 (g, h)) also show a slight wind shear inversion at higher altitudes.

~~Within a cluster, the wind speed profiles span a fairly narrow range of wind speeds indicating coherent clusters. Figure 7 shows the distribution of wind speed profiles within each of the clusters.~~

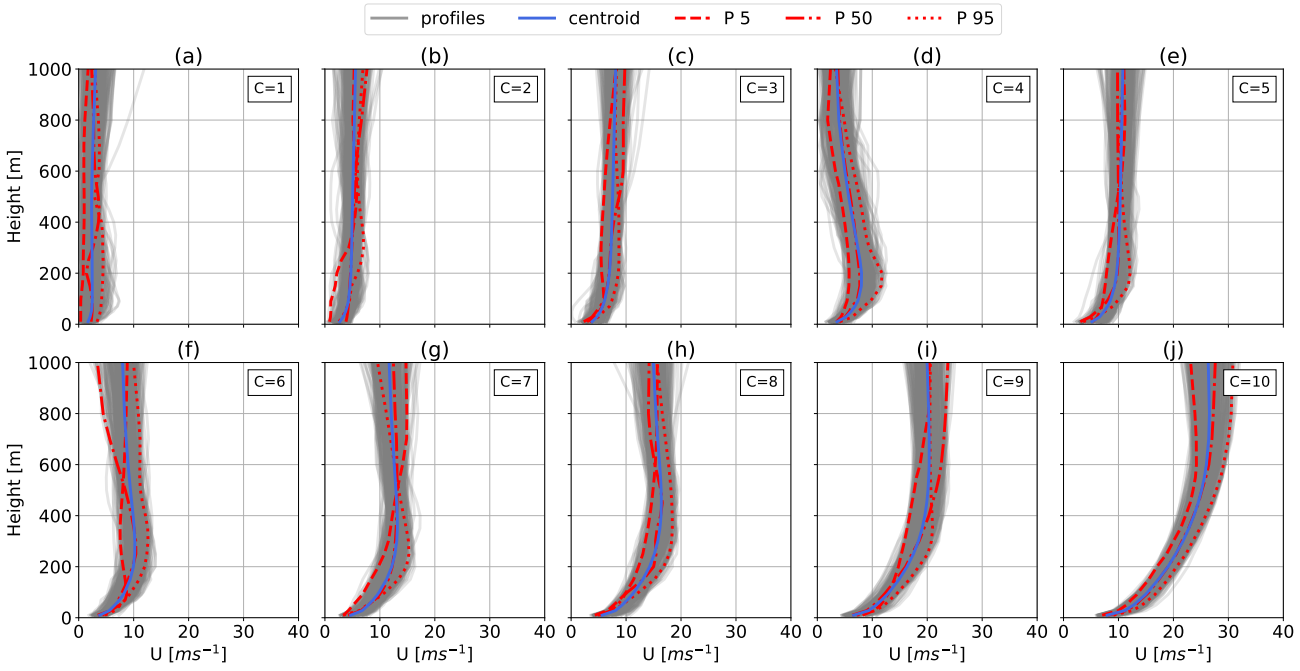

Figure 7. Vertical onshore ~~wind speed profiles~~ U categorized ~~into k = 10 clustered~~ using the k-means clustering algorithm. ~~Later~~ The analyses ~~use k~~ in Section 6 employ k = 20 clusters. Here k = 10 is chosen for visualization purposes. The average profile (centroid) is shown in blue and the profiles associated with this cluster are shown in gray. Clusters 1 to 10 (a-j) are sorted and labeled in ascending order of average centroid ~~wind speed~~ $\overline{U}(z_{\mathrm{ref}})$ between 100 m and 400 m. The corresponding cluster frequency ~~f~~ f for each cluster ~~C~~ C is shown in Figure 6. The ~~red lines mark~~ in the ~~wind speed profile~~ optimization toolbox implemented U are highlighted with ~~the 5th, 50th and 95th percentiles of average wind between 100 and 400 m within each cluster~~a red line.

~~The clusters~~ Clusters C = 1 (a) to C = 10 (j) are sorted by the average centroid (blue line) wind speed between ~~$U(z_{\mathrm{ref}} = 100 - 400$ m)~~$\overline{U}(z_{\mathrm{ref}})$. The red lines indicate the ~~profile~~ profiles associated with the 5th, 50th and 95th ~~percentiles of $U(z_{\mathrm{ref}})$~~ percentile of $\overline{U}(z_{\mathrm{ref}})$ within each cluster. To reduce computational cost, only these profiles are later implemented into the ~~awebox optimization framework. We chose~~ `awebox` optimization toolbox. We selected these profiles because they are less likely to be ~~an irregular outliers of~~ irregular outliers than the extrema of the cluster, while still representing the variation within their respective cluster~~than the cluster's extrema. Furthermore, these profiles describe the in-cluster variation with respect to wind speed and profile shape. The focus of this study is the investigation of AWES performance subject to realistic wind conditions, which is why we opted against using averaged or scaled data,~~ . These profiles illustrate the variations within their respective cluster and are not average profiles like the cluster centroids or scaled or semi-empirical approximations such as the ~~cluster centroids or~~

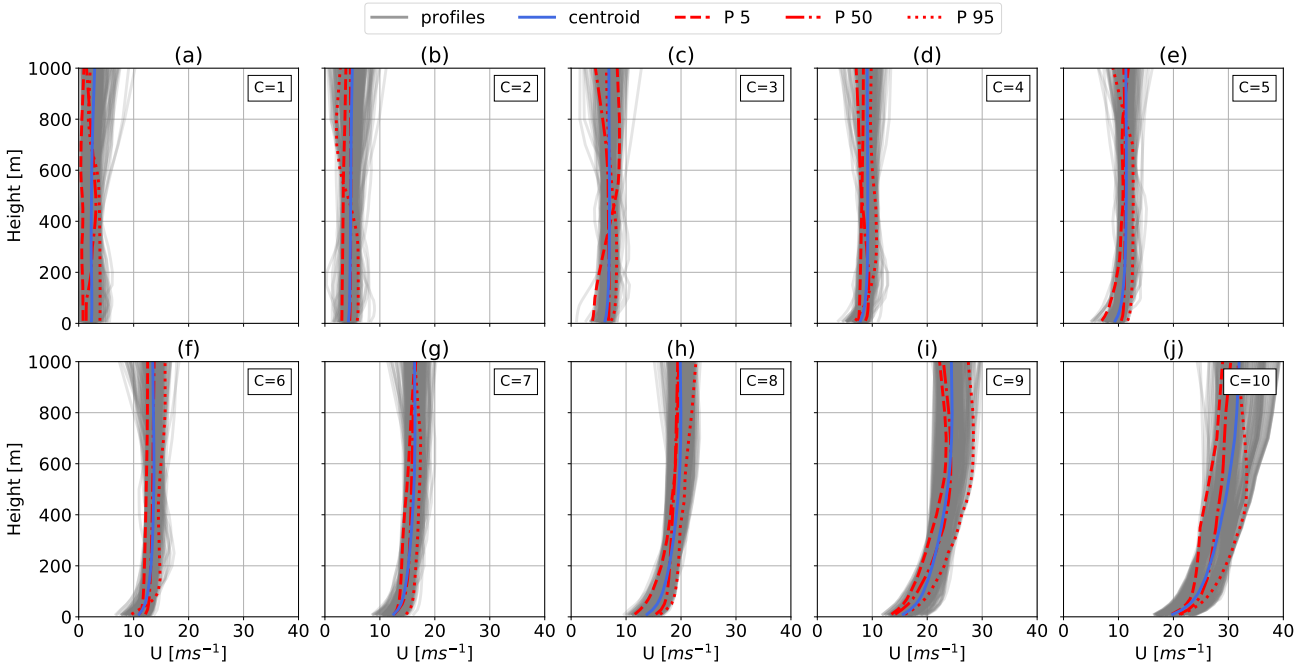

Figure 8. Vertical offshore wind speed profiles categorized using the *k*-means clustering algorithm. The analyses in Section 6 employ k = 20 clusters. Here k = 10 is chosen for visualization purposes. The average profile (centroid) is shown in blue and the profiles associated with this cluster are shown in gray. Clusters 1 to 10 (a-j) are sorted and labeled in ascending order of average centroid $\overline{U}(z_{\mathrm{ref}})$ between 100 m and 400 m. The corresponding cluster frequency f for each cluster C is shown in Figure 6. The in the optimization toolbox implemented U are highlighted with a red line.

~~normalized wind speed profiles. The equivalent offshore clusters can be found in Figure 8 in the appendix.~~ logarithmic wind profile. Evidently, the ~~wind speed magnitude~~ magnitude of the wind speed plays a dominant role in the clustering process. ~~This can lead to profiles with different shapes to be assigned to the same cluster due to similar average wind speed.~~ A clearer wind profile shape distinction could be achieved by normalizing the data before clustering it (Molina-García et al., 2019; Schelbergen et al., 2020).

2.5 Analysis of clustered statistics

This subsection ~~investigates the correlation between~~ examines the relationship between the clusters and monthly~~(Figure 9), diurnal(Figure 10)~~ , diurnal, and atmospheric stability~~(Figure 11) for the onshore (top row) and offshore (bottom row) location. This reveals patterns within the clusters, gives an~~ . These analyses reveal patterns that give insight into the wind regime and ~~informs AWES performancefor a given time and location. Here only *k*~~ the resulting changes in AWES performance. Subsequent sections examine wind data from k = 20 clusters, while here only k = 10 clusters are chosen for presentation purposes~~, but wind~~

~~data from k = 20 will be investigated in later sections~~. Clusters are sorted in ascending order of average centroid wind speed ~~$U(z_{\mathrm{ref}} = 100 - 400\ \mathrm{m})$~~ $\overline{U}(z_{\mathrm{ref}} = 100 - 400\ \mathrm{m})$ and color coded ~~accordingly. The corresponding centroids are shown in Figure~~ as in Figure 5 and Figure 6.

Both locations ~~follow a distinct annual pattern (Figure 9). Profiles associated with high~~ exhibit a clear annual pattern as shown in Figure 9. High wind speeds are more ~~likely during the winter months and profiles with~~ common during winter while low wind speeds are ~~predominantly found~~ more prevalent in summer. This is likely due to the seasonal difference in surface heating and the resulting differences in atmospheric mixing. The two onshore and offshore clusters associated with the highest wind speed are almost exclusively present during November to February.

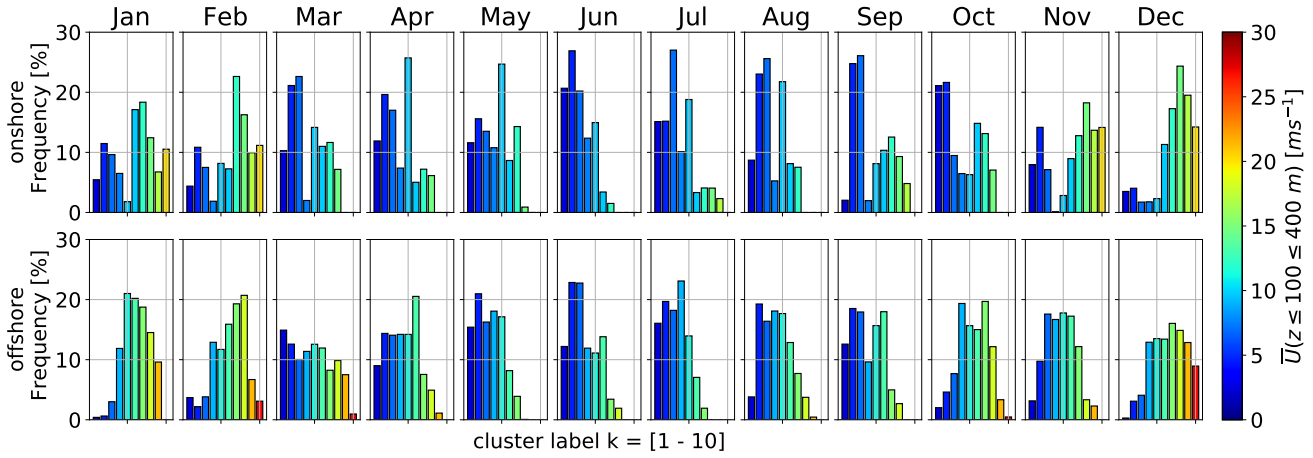

Figure 9. Monthly frequency of ~~k-means~~ k-means clustered onshore (top) and (offshore) wind velocity profiles **U** for a representative ~~k~~ k = 10. All clusters are sorted and color coded according to their ~~average wind speed between 100 and 400 m~~$\overline{U}(z_{\mathrm{ref}} = 100 - 400\ \mathrm{m})$. The corresponding centroid associated with each cluster can be found in Figure 6.

Offshore data ~~shows almost no diurnal variation (Figure 10)~~ indicate minimal diurnal variation as shown in Figure 10, with only a slight increase ~~of clusters associated with lower wind speeds during daytime~~in the frequency of lower wind speed clusters during the day.Onshore clusters, on the other hand, are more dependent on the diurnal cycle with a higher likelihood of ~~low speed~~ low-speed clusters after sunrise. The frequency of onshore cluster 4, which ~~comprises~~ includes a LLJ nose (Figure 6), ~~drops~~ decreases to almost zero during ~~daytime and increases during nighttime, substantiating the assumption~~ the day and rises at night, supporting the notion that this cluster is ~~associated with~~ linked to nocturnal LLJs.

~~The~~ Thwe wind velocity clusters ~~correlate with atmospheric stability as expected~~ (Figure 11) show a correlation with atmospheric stability. Low wind speed clusters make up about 20% to 30% of the annual wind resource. These clusters exhibit Obukhov lengths close to zero (~~likely~~ probably caused by very low friction velocity u_*) and are classified as "other" ~~because they do not fall within one of the other atmospheric stability classes according to (Floors et al., 2011)~~ according to Floors et al. (2011) (Table 2). Unstable (U) and near unstable (NU) conditions are associated slightly higher wind speeds. The

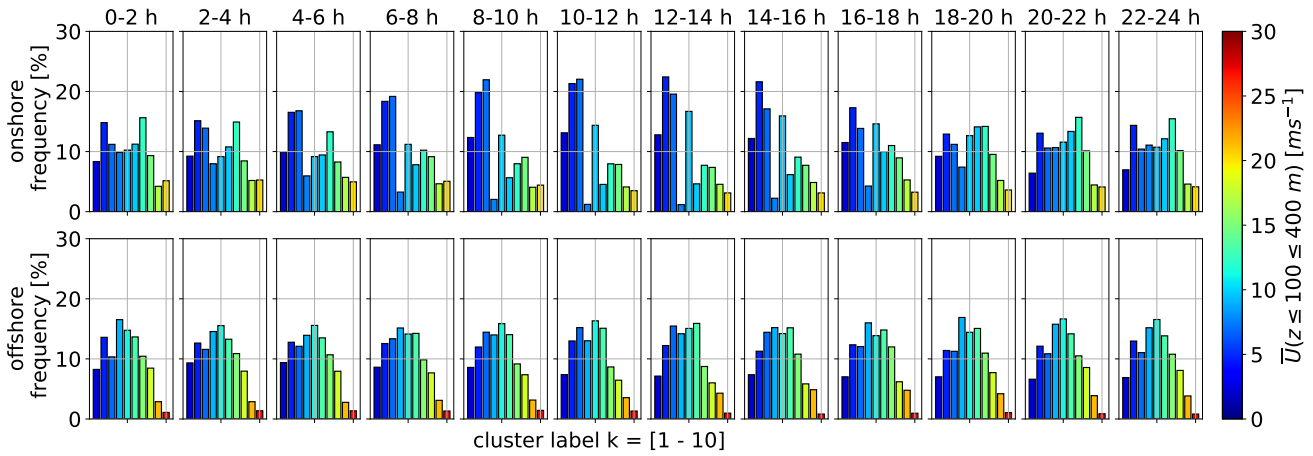

Figure 10. Diurnal frequency of ~~*k*-means~~ k-means clustered onshore (top) and (offshore) wind velocity profiles $\mathbf{U}$ for a representative ~~*k*~~ k = 10. All clusters are sorted and color coded according to their ~~average wind speed between 100 and 400 m~~$U(z_{\text{ref}} = 100 - 400\ \text{m})$. The corresponding centroid associated with each cluster can be found in Figure 6.

highest wind speeds develop during neutral (N) and near stable (NS) conditions. It ~~needs to~~ should be acknowledged that strong winds driven by large pressure gradients can lead to neutral stratification. LLJ profiles associated with onshore cluster 4 are most likely to develop during stable (S) and very stable (VS) conditions.

In ~~conclusion, *k*-means clustering is able to capture and reveal temporal variations in the wind regime as well as location specific wind profile shapes~~ summary, k-means clustering can effectively group wind velocity profiles with similar characteristics up to high altitudes. ~~Wind speed magnitude seems to determine~~ These clusters are correlated with seasonal and diurnal changes as well as atmospheric stability. The magnitude of the wind velocity profiles appears to have a greater impact on the resulting clusters ~~more than profile shape . Less~~ than the shape of the profile. The algorithm is able to identify less common, non-monotonic profile shapes, for example profiles with LLJs, can be identified. Normalizing the profiles before clustering ~~will give more insight into the different vertical profile shapes , but is not pursued in the present study. The cluster frequency reflects the expected temporal and atmospheric stability classification.~~ can provide more information about the different shapes of the vertical profiles, but this was not done in this study.

3 Dynamic AWES model

This section introduces the dynamic AWES model used in the `awebox` trajectory optimization ~~framework (De Schutter et al., 2020) . Sub-section 3.1 gives an overview~~ toolbox (De Schutter et al., 2020). Subsection 3.1 provides a summary of the system configuration. The ~~following Sub-sections introduce the aerodynamic model (Sub-section 3.2),~~ aerodynamic model is presented in Subsection 3.2, while the aircraft mass model ~~(Sub-section 3.3)~~is introduced in Subsection 3.3.

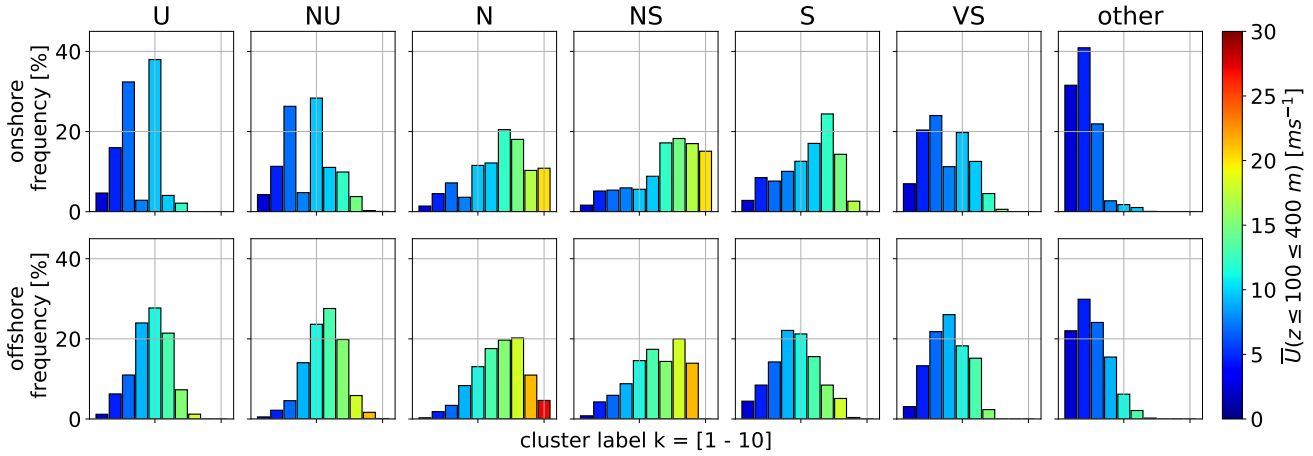

Figure 11. Atmospheric stability (U: unstable, NU: nearly unstable, N: neutral, NS: nearly stable, S: stable, VS: very stable) distribution of ~~*k*-means~~ k-means clustered onshore (top) and (offshore) wind velocity profiles U for a representative ~~*k*~~ k = 10. The associated stability classes are based on Obukhov length (Table 2). All clusters are sorted and color coded according to their ~~average wind speed between 100 and 400 m~~$U(z_{\mathrm{ref}} = 100 - 400\ \mathrm{m})$. The corresponding centroid associated with each cluster can be found in Figure 6.

3.1 Model configuration

The rigid-body model considers a ~~6 degree~~ six degrees of freedom (DOF) ~~rigid-wing~~ fixed-wing aircraft which is connected to the ground via a straight tether. ~~By introducing the tether , the DOF is reduced to 5, a minimized set of generalized coordinates. It uses precomputed quadratic approximations of~~ The introduction of the tether reduces the DOF to five (**?**). The model uses precomputed second order polynomials to describe the aerodynamic coefficients (Subsection 3.2) which are controlled via aileron-, elevator- and rudder-deflection ~~rates (Malz et al., 2019). The longitudinal motion~~ (Malz et al., 2019).

The longitudinal dynamics of the tether is controlled via the tether jerk $\dddot{l}$ from which the tether acceleration $\ddot{l}$, reeling speed $\dot{l}$ and length l are determined. The tether is modeled as a single solid rod which ~~cannot support compressive forces~~ neither supports compressive forces nor bending moments (De Schutter et al., 2019). The rod is divided into ~~$n_{\mathrm{aero}} = 10$~~ 10 segments. Tether drag is calculated individually for each segment, using the local apparent wind speed (Bronnenmeyer, 2018). The tether drag of every segment is equally ~~divided~~ distributed between the two endpoints~~and propagated to either the aircraft or ground station~~. This leads to an underestimation of total tether drag at the ~~aircraft. Refer to (Leuthold et al., 2018)for more details~~kite (Leuthold et al., 2018). The ground station ~~itself is not explicitly modeled , but implemented as~~ dynamics are not modeled explicitly, but are implemented using a set of constraints.

These constraints serve as an example of a system rather than representing a fully optimized design. A reel-in speed of $\dot{l}_{\mathrm{in}} = 15\ \mathrm{ms}^{-1}$ and reel-out speed of $\dot{l}_{\mathrm{out}} = 10\ \mathrm{ms}^{-1}$ are ~~chosen, resulting~~ assumed to be realistic winch motor constraints based on information provided by a ground station manufacturer and literature review. This results in a reel-out to reel-in

ratio of $\frac{2}{3}$ ~~which is assumed to be within design limitations of the winch~~. A maximum tether acceleration of $\ddot{l} = 20\ \mathrm{ms}^{-2}$ is imposed to comply with generator torque limits. The tether diameter is ~~chosen such that the maximum tether tension is about $F^{\max}_{\text{tether}} = 50$ kN with a~~ selected to be able to withstand three times (safety factor of SF = ~~3.~~ 3) the maximum tether tension of $F^{\max}_{\text{tether}} = 50$ kN. This results in a rated average cycle power of about $P_{\text{rated}} \approx 260 - 300$ kW, according to `awebox` simulations. ~~These ground station and tether constraints do not represent a fully optimized design, but rather an example system.~~

3.2 Aerodynamic model

The presented model utilizes the Ampyx Power AP2 aerodynamic coefficients from De Schutter et al. (2020); Malz et al. (2019); Ampyx (2020). The AP2 reference is scaled ~~to a wing area of~~ from a projected wing surface area of $A_{AP2} = 3\ \mathrm{m}^2$ to $A = 20\ \mathrm{m}^2$, to generate results for more realistic and probable devices, while the aspect ratio is kept constant at $AR = 10$. The total ~~drag coefficient $c_{\mathrm{D,total}}$~~ combined drag coefficient of the aircraft and tether ~~highly depends on tether drag and therefore~~ $c_{\mathrm{D,total}}$:

$$c_{\mathrm{D,total}} = c_{\mathrm{D,kite}} + \frac{1}{4}\frac{ld}{A} c_{\mathrm{D,tether}}. \tag{2}$$

depends on the diameter d and length l of the tether, as well as the ~~wing~~ projected surface area A and the aerodynamic drag coefficient ~~of the wing $c_{\mathrm{D,wing}}$~~$c_{\mathrm{D,kite}}$ of the kite. To illustrate the effect of a longer tether, we utilize a simple tether drag estimation ~~and visualize the aerodynamic coefficients for tether lengths up to $l = 1000$m in Figure 12.~~

~~Ampyx AP2 reference wing aerodynamic lift c_{L} (a) and drag $c_{\mathrm{D,total}}$ coefficients (b) (Malz et al., 2019; Ampyx, 2020), including tether drag according to Equation (2), for a wing area A of $20\mathrm{m}^2$ and tether diameter of $d = 7.8$mm (Table 3. Tether length varies between 250 m and 1000 m. (c) shows the pitch moment coefficient c_{m} as a function of angle of attack. The bottom figures display lift over drag (d), lift-to-drag ratio over angle of attack (e) and $c^3_{\mathrm{R}}/c^2_{\mathrm{D,total}}$ over angle of attack (Loyd, 1980).~~

~~We consider a straight,~~ for a cylindrical tether with constant diameter and an aerodynamic tether drag coefficient $c_{\mathrm{D,tether}}$ of 1.0~~, which~~. This value would be even higher for braided tethers. Assuming a ~~uniform wind~~constant and uniform wind speed, the line integral along the tether results in a total effective drag coefficient of ~~:~~

$$c_{\mathrm{D,total}} = c_{\mathrm{D,wing}} + \frac{1}{4}\frac{ld}{A} c_{\mathrm{D,tether}}$$

~~See Houska and Diehl (2007); Argatov and Silvennoinen (2013)~~ $ld/4A$ accounts for the different reference areas for $c_{\mathrm{D,kite}}$ and $c_{\mathrm{D,tether}}$. See Houska and Diehl (2007), Argatov and Silvennoinen (2013) and van der Vlugt et al. (2019) for details. Figure 12 visualized the tether drag impact on the aerodynamic coefficients for tether lengths up to $l = 1000$ m.

~~We approximate the wing's~~

The lift coefficient c_{L} (Figure 12 ~~a) by a quadratic function~~ (a)) is approximated as a second-order polynomial function of angle of attack α, to simulate stall effects. A ~~single~~ polynomial description is necessary for the entire range of angle of attack,

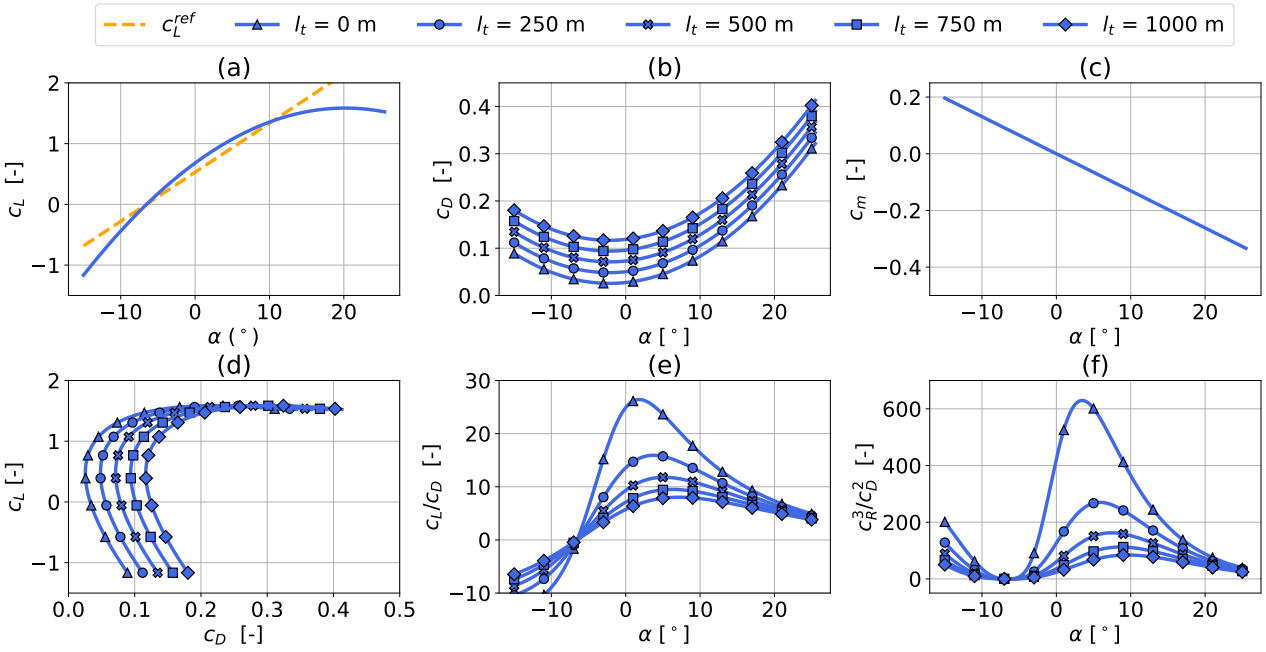

Figure 12. Ampyx Power AP2 reference kite aerodynamic lift c_L (a) and drag $c_{D,total}$ coefficients (b) (Malz et al., 2019; Ampyx, 2020), including tether drag according to Equation (2), for a projected wing surface area $A = 20\ m^2$ and tether diameter of $d = 7.8\ mm$. Tether length varies between 250 m and 1000 m. (c) shows the pitch moment coefficient c_m as a function of angle of attack α. The bottom figures display lift over drag (d), glide ratio over angle of attack (e) and $c_R^3/c_{D,total}^2$ over angle of attack.

as the optimization algorithm requires a ~~two times~~ two-times differentiable function. For the sake of simplicity, a piecewise, continuous and differentiable function has not been implemented. As a result, the implemented c_L (blue) slightly exceeds the linear (orange) lift coefficient c_L^{ref} of the AP2 reference (Malz et al., 2019) between $-5 \leq \alpha \leq 10°$. The side slip angle β is included in the model, but variation of aerodynamic coefficients due to β are neglected. The pitch moment (Figure 12 ~~e~~(c)) is assumed to behave linearly~~and changes~~. Changes in the drag coefficient (Figure 12 ~~b~~(b)) are approximated by a ~~quadratic function~~second-order polynomial. Tether drag is independent of ~~aircraft angle of attack~~ α and therefore added to the zero-lift drag coefficient~~c_{D0}. c_R represents the~~. The resultant aerodynamic force coefficient ~~:~~

c_R is represented as

$$c_R = \sqrt{c_L^2 + c_{D,total}^2}. \tag{3}$$

~~The optimal~~ The drag polar in Figure 12 (d) depicts the relationship between the kite's lift coefficient c_L and total drag coefficient $c_{D,total}$ for the tethered aircraft. The maximum values of the glide ratio ~~$c_L/c_{D,total}$~~ $c_L/c_{D,total}$ (Figure 12 ~~e) and aerodynamic factor~~ (e)) and the ratio $c_R^3/c_{D,total}^2$ (Figure 12 ~~f~~(f)) which is one of the main determining factors of AWES power ~~(Schmehl et al., 2013; Loyd, 1980)~~(Loyd, 1980; Schmehl et al., 2013), decrease significantly with tether length and shift towards higher angles of attack. ~~This effect is less pronounced for larger wings because~~ The impact of tether drag on the total

drag coefficient is less significant for larger kites because its impact decreases with the size of the ~~effect of tether drag reduces when scaling up to larger~~ aircraft.

3.3 Aircraft mass model

The aircraft dynamics are described by a single rigid body of mass ~~m_{aircraft}~~ m_{kite} and moment of inertia $\mathbf{J}$, ~~with~~ subject to aerodynamic forces and moments~~applied to it. m_{aircraft}~~. The inertial properties m_{kite} and $\mathbf{J}$ are determined by upscaling the AP2 reference ~~wing from $A_{\text{wing}}^{\text{AP2}} = 3\ \text{m}^2$~~ kite from $A_{\text{AP2}} = 3\ \text{m}^2$ to $A = 20\ \text{m}^2$. ~~Mass~~ The mass m_{scaled} and moment of inertia $\mathbf{J}_{\text{scaled}}$ of a ~~rigid-wing aircraft scale relative to~~ fixed wing aircraft scale as functions of the wing span b and aspect ratio AR, which is kept constant and its impact on scaling is neglected here, with a mass-scaling exponent κ ~~.~~ (?)

$$m_{\text{scaled}} = m_{\text{ref}} \left(\frac{b}{b_{\text{ref}}} \right)^{\kappa}, \tag{4}$$

$$\mathbf{J}_{\text{scaled}} = \mathbf{J}_{\text{ref}} \left(\frac{b}{b_{\text{ref}}} \right)^{\kappa+2}. \tag{5}$$

Pure geometric scaling of solid bodies, in contrast to aircraft structures that use a lightweight structural frame, corresponds to Galileo's square-cube law with $\kappa = 3$. In reality, as has been seen for the development of conventional WTs, design and material improvements occur over time. ~~A~~ An appropriate mass-scaling factor was determined based on a review of the available literature~~containing system mass details was conducted to identify an appropriate mass-scaling factor. The results are shown in Figure 13 depicting actual and anticipated AWES scale bounded by $\kappa = 2.2 - 2.6$ (gray area)~~. Figure 13 depicts actual (circle) and anticipated (square) aircraft mass scaling provided by Makani (red color scheme) and Ampyx Power (blue color scheme). The diamond shaped data points (green color scheme) are scaled up versions of Ampyx Power prototypes used in several research papers (Haas et al., 2019; Eijkelhof et al., 2020; ?). The gray area encompasses most of the data points with $\kappa = 2.2 - 2.6$. We chose $\kappa = 2.4$ based on a curve fit of the available published sizing study data. This ~~seems quite ambitions and might be achievable for soft wing kites~~appears to be an ambitious goal for rigid kites, but attainable for flexible ones. The mass of these hollow tensile structures filled with air mostly scales the wing surface area, leading to significantly lower mass-scaling exponents and more beneficial mass-scaling. ~~A scaling study (Sommerfeld et al., 2020) which has been written in parallel to this paper investigates~~ ? examined the impact of ~~variable mass-scaling exponents~~various size, mass, and aerodynamic scaling factors on performance.

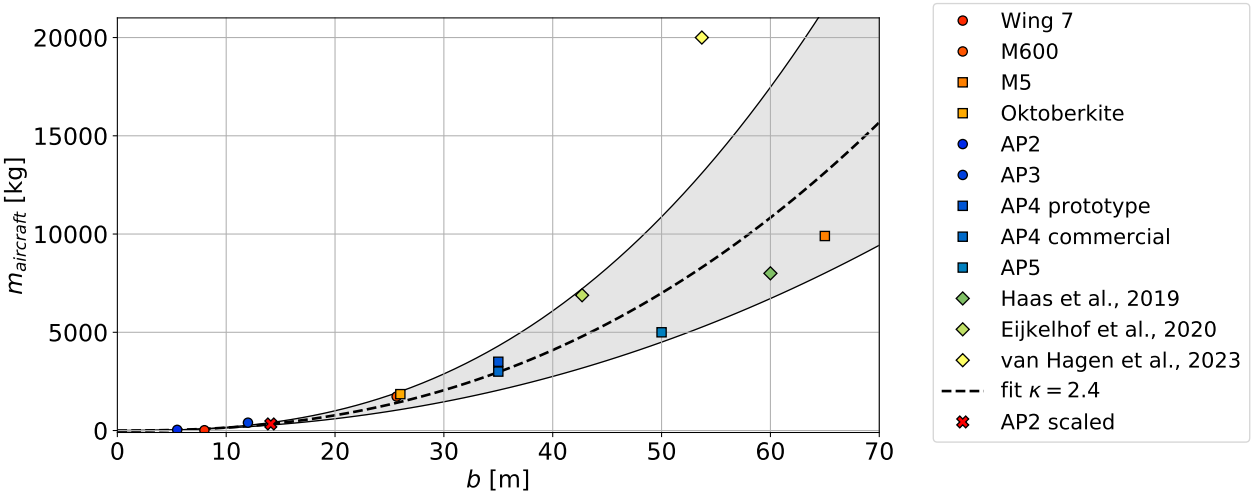

Figure 13. ~~Curve fit of published sizing studies~~ Published actual (circle) and anticipated (square) aircraft mass ~~(Haas et al., 2019; Kruijff and Ruiterkamp, 2018; Eijkelhof et al., 2020; Ampyx, 2020; Echeverri et al., 2020)~~scaling provided by Makani (red color scheme) (Echeverri et al., 2020) and Ampyx Power (blue color scheme) (Ampyx, 2020; Kruijff and Ruiterkamp, 2018). Diamond shaped data (green color scheme) depict the mass of scaled up versions of Ampyx Power prototypes used in research papers (Haas et al., 2019; Eijkelhof et al., 2020; **?**). For ~~these~~ most data, mass scales ~~within~~ with a scaling exponent ~~range of~~ between $\kappa = 2.2 - 2.6$ (gray area). The chosen mass-scaling exponent of $\kappa = 2.4$ is represented by a dashed line and the investigated scaled AP2 design is highlighted by a ~~black square~~red X.

4 Optimal control ~~Model~~model

AWES need to dynamically adapt to changing wind conditions to ~~optimize~~ maximize power generation and ensure save operation. ~~This section~~ Subsection 4.1 introduces the dynamic trajectory optimization ~~awebox toolbox (De Schutter et al., 2020) (Sub-section 4.1) and describes~~ toolbox `awebox` (De Schutter et al., 2020). We describe the most important boundary ~~(Sub-section 4.2)~~ conditions in Subsection 4.2 and initial conditions ~~(Sub-section 4.3. Sub-section~~ in Subsection 4.3. Subsection 4.4 explains the implementation of the previously described wind profiles ~~. A polynomial fit through the simulated data points is needed, as the gradient-based optimizer requires an at least two times differntiable function.~~ (Section 2).

4.1 AWES model overview

~~Only one production cycle, including reel-in and reel-out, is optimized. Take-off and landing are not considered.~~ Maximizing the average cycle power can be formulated as an trajectory optimization problem~~which combines~~ , which takes into account the interaction between ~~tether, flying wing~~ the tether, kite, and ground station. This study analyzes the mechanical power produced by a single ~~tethered aircraft~~ aircraft tethered with a straight ~~tether~~line throughout one production cycle, including

reeling in and out, while disregarding take-off and landing. Power production is intrinsically linked to the aircraft's flight dynamics, as the AWES never reaches a steady state over the course of a power cycle. Generating dynamically feasible and power-optimal flight trajectories is nontrivial, given the nonlinear and unstable system dynamics and the presence of ~~nonlinear~~ various flight envelope constraints. Optimal control methods are a natural candidate to tackle ~~these~~ such problems, given their inherent ability to deal with nonlinear, constrained multiple-input-multiple-output systems (De Schutter et al., 2019; Leuthold et al., 2018). This trajectory optimization is a highly nonlinear and non-convex problem which can have multiple local optima~~, depending on initialization~~. The initial and final ~~state~~ states of each trajectory ~~are freely chosen by the optimizer but~~ must be equal to ensure periodic operation but are freely chosen by the optimizer. In periodic optimal control, an optimization problem is solved by computing periodic system ~~state and control trajectories that optimize~~ states and control inputs that maximize a performance index (here average power output $\overline{P}$) while satisfying the system's dynamic equations ~~. We apply this methodology to WRF-simulated wind speed profiles to generate a range~~ and constraints. We use this approach to generate a variety of realistic trajectories ~~. The temporal development of important operational parameters is illustrated to better understand instantaneous performance and estimate average cycle power.~~ from WRF-simulated wind velocity profiles. Any wind data sets, such as wind atlas data, LiDAR or met mast measurements can be implemented into the optimization model via a ~~twice~~ two-times differentiable function, depending on the scope and purpose of the investigation.

4.2 Constraints

Several important constraints define the operational envelop. The most important constraints such as tether length, ~~speed and~~ tether reeling speed and tether force are summarized in Table 3. The following constraints define a representative and not ~~optimized AWESdesign.~~ design-optimized AWES. The power of ~~ground generation~~ ground-generation AWES is limited by the tether force, which is defined by the tensile strength ~~($\sigma_{\max}^{\text{tether}}$)~~ and tether diameter d, and the tether ~~speed~~reeling speed $\dot{l}$. The tether diameter is chosen such that the maximum tether tension is ~~about~~ approximately $F_{\text{tether}}^{\max} = 50$ kN with ~~a~~ an additional safety factor of SF = 3. This ~~results~~ produces a peak power of ~~$P_{\text{peak}} \approx 500$kW, assuming~~ $P_{\text{peak}} \approx 500$ kW, with a maximum reel-out speed of $\dot{l} = 10\ \text{ms}^{-1}$. This corresponds to a rated average cycle power of approximately $P_{\text{rated}} \approx 260 - 300$ kW. We assume a reel-out to reel-in tether reeling speed ratio of $\frac{2}{3}$ to be within winch design limitations. The tether length constraint is ~~very loos~~relatively lenient, to allow the optimizer to investigate a wide range of possible operating heights ~~. We assume a reel-out to reel-in ratio of $\frac{2}{3}$ to be within winch design limitations. Flight envelope constraints include limitation of aircraft~~z_{oper}. The flight envelope is constrained by limitations on the aircraft's acceleration, roll and pitch ~~angle (to avoid~~ angles (to prevent collision with the tether)~~and~~ , as well as the angle of attack ~~. Furthermore, a~~ α and side slip angle β. A minimal operating height of ~~$z_{\min} = 50 + \frac{A_{\text{wing}}}{2}$ m~~ $z_{\min} = 50\ m + \frac{b}{2}$ is imposed for safety reasons.

4.3 Initialization

The ~~results generated by the~~ trajectory optimization process is highly nonlinear and non-convex~~trajectory optimization can have~~ , resulting in multiple local optima. These solutions ~~, for which only local optimality can be guarantied,~~ depend on the chosen

Table 3. Selected AWES design parameters for the original AP2 reference system (Malz et al., 2019) and the scaled up $A = 20\ \mathrm{m}^2$ design, analyzed in this study. Values in square brackets represent the upper and lower bounds, which are implemented as inequality constraints.

Parameter		AP2	design 1
Aircraft	A [m^2]	3	20
	~~c_{wing}~~ c_{kite} [m]	0.55	1.42
	~~b_{wing}~~ b_{kite} [m]	5.5	14.1
	AR [-]	10	10
	~~m_{aircraft}~~ m_{kite} [kg]	36.8	355
	α [°]		[-10 : 30]
	β [°]		[-15 : 15]
Tether	l [m]		[1: 2000]
	$\dot{l}$ [ms^{-1}]		[-15 : 10]
	$\ddot{l}^{\mathrm{max}}$ [ms^{-2}]		[-10 : 10]
	d [mm]		7.3
	$\sigma_{\mathrm{max}}^{\mathrm{tether}}$ [Pa]		3.6×10^9
	SF [-]		3
Operational	z_{min} [m]		60
	α [°]		[-10 : 20]
	β [°]		[-5 : 5]

~~initialization~~initial conditions. Some of ~~these local optima can have unwanted characteristics , which is why~~ the locally optimal solutions may be feasible and within the constraints, but may have undesirable characteristics such as looping maneuvers during reel-in or excessively high operating altitudes. As a result, it is necessary to evaluate the quality of all solutions~~needs to be evaluated a posteriori~~. To solve ~~this complex~~ the complex optimization problem, initial guesses are generated using a homotopy technique similar to Gros et al. (2013). ~~The homotopy~~ This technique initially fully relaxes the dynamic constraints using fictitious forces and moments to reduce model nonlinearity and coupling, ~~improving~~ which improves the convergence of Newton-type optimization techniques. The constraints are then gradually re-introduced until the relaxed problem matches the original problem. ~~The~~ The trajectory optimization is initialized with a circular trajectory in downwind direction (positive x direction) with a fixed number of n_{loop}= ~~five loops~~ 5 loop maneuvers at a 30° elevation angle, an initial tether length $l_{\mathrm{init}} = 500$ m ~~, in positive x direction~~ and an estimated aircraft speed of $v_{\mathrm{init}} = 10\ \mathrm{ms}^{-1}$ along entire initial trajectory. This initialization is kept constant for all ~~wind speed~~ vertical wind velocity profiles. The number of ~~loops~~ loop maneuvers is not part of the objective function and ~~does therefore not change with wind speed. The~~ remains unchanged during all optimization runs. Further investigation is needed to determine the impact of the number of loops~~needs to be investigated further, but previous analyses showed that the `awebox`-estimated~~ . However, previous analyses have shown that the average cycle power ~~is rather insensitive to~~ estimated by `awebox` is relatively unaffected by the number of loops. It is likely beneficial to reduce the number

of loops with wind speeds because ~~higher wind speeds~~ the system can reel out faster at higher wind speeds and reach maximum tether length faster.

4.4 Wind profile implementation

~~This study investigates WRF-simulated wind data, instead of assuming a wind profile relationship such as the logarithmic or exponential wind profile. These relationships do not appropriately represent wind conditions above earth's surface layer (Optis et al., 2016) and cannot emulate the variety of non-monotonic and non-logarithmic wind profiles which occur at both locations. This is particularly important for AWES which can benefit from and need to be able to operate in these conditions.~~

To reduce the computational cost while maintaining an adequate representation, ~~we~~ only implement three wind velocity profiles from each cluster into the trajectory optimization ~~framework~~toolbox. More profiles could be chosen for an in-depth analysis. ~~A total~~ The power for a total number of 60 wind profiles, three profiles for each of the ~~k~~ k = 20 clusters (Section 2.3), for each location are ~~optimized~~maximized. The three selected profiles correspond to the 5th, 50th and 95th percentiles of average wind speed ~~$U(z_{\text{ref}} = 100 - 400$ m)~~ $\overline{U}(z_{\text{ref}} = 100 - 400$ m) within each cluster. We assume that these profiles represent the cluster's spectrum of wind conditions at operating height ~~.~~z_{oper}. The `awebox` includes a simplified atmospheric model based on international standard atmosphere to account for air density variation.

The ~~longitudinal u and lateral v wind components of the sampled WRF-simulated wind profiles~~ vertical wind velocity profiles $\mathbf{U}'$ are rotated such that the main wind direction~~u_{main}~~, which is defined as the average ~~wind~~ direction between 100 and 400 m , ~~is pointing~~ points in positive x direction ~~and the transverse component u_{dev}~~ (Figure 4). As a result the wind velocity components at every height consist of a main component u in x direction and transverse component v in y direction. ~~This is equivalent to assuming omnidirectional operation.~~ The results can be seen in hodographs of Figure 14 (c) and Figure 15 (c).

The `awebox` toolbox uses the gradient-based MA57 solver (HSL, 2020) in IPOPT (Waechter and Laird, 2016) to solve the ~~non-linear~~ nonlinear control problem. Therefore, it is necessary to interpolate the vertical wind velocity profiles with a twice continuously differentiable ~~function~~functions. We chose to use Lagrangian polynomials (Abramowitz and Stegun, 1965) because the resulting polynomials pass through the input data points. To avoid over fitting a limited number of data points are implemented. These data points are chosen based on the anticipated ~~operating height~~z_{oper}, to best represent the wind conditions at relevant heights.

For comparison, logarithmic wind speed profiles,

$$U_{\log} = U_{10}\left(\frac{\log_{10}(z/z_0)}{\log_{10}(z_{10}/z_0)}\right) \tag{6}$$

with a roughness length of $z_0^{\text{onshore}} = 0.1$ and $z_0^{\text{offshore}} = 0.001$, are implemented into the trajectory optimization ~~framework~~ toolbox.

$$U_{\log} = U_{\text{ref}}\left(\frac{\log_{10}(z/z_0)}{\log_{10}(z_{\text{ref}}/z_0)}\right).$$

The reference wind speed ~~$U_{\mathrm{ref}},$~~ U_{10} at reference height ~~$z_{\mathrm{ref}} = 10$ m,~~ $z_{10} = 10$ m varies from 3 to 20 ms^{-1} with a step size of ~~$\Delta U_{\mathrm{ref}} = 1\ \mathrm{ms}^{-1}$. The `awebox` includes a simplified atmospheric model based on international standard atmosphere to account for air density variation.~~ $\Delta U_{10} = 1\ \mathrm{ms}^{-1}$.

5 Reference models

This section ~~introduces reference models used in Section 6 to analyze and contextualize the optimization results. To compare the optimization results to analytic solutions, we define a~~ establishes a simplified quasi-steady-state AWES reference model (QSM) (~~Sub-section~~ Subsection 5.1) and a steady-state WT model (~~Sub-section 5.2)~~ Subsection 5.2) to compare the results of the optimization with analytical solutions.

5.1 AWES reference model

The QSM estimates the mechanical power of ~~ground generation~~ ground-generation AWES based on the assumption that the trajectory of the tethered aircraft can be approximated by a progression through steady equilibrium states where tether tension and total aerodynamic force are aligned. We simplify the QSM by approximating the reel-out and reel-in trajectory with a single state and neglecting the effects of gravity. The QSM, based on Argatov et al. (2009) and generalized by Schmehl et al. (2013) and van der Vlugt et al. (2019), approximates the aircraft as a point mass. Its position is described in ~~the spherical coordinatesby the~~ terms of spherical coordinates, i.e. the radial distance from the ground station, the elevation angle ε and azimuth angle ϕ relative to the direction of the mean wind velocity vector ~~U~~ $\mathbf{U}$. For lightweight soft-wing kites, this is a reasonably good approximation because the low mass of the kite leads to very short acceleration times. The model includes losses caused by the misalignment of the tether and wind velocity vector. The same ~~model parametersand constraints of the optimization model also~~ design parameters, system constraints and wind conditions (Section 2(apply to the ~~QSM reference model (see Sub-section 4.2)~~ optimization model (Subsection 4.2) as well as the QSM reference model. presented in We maximize the cycle average power P_{QSM} by varying l, $\dot{l}$ and z and assuming an optimal ratio $c_{\mathrm{R}}^3/c_{\mathrm{D,total}}^2$.

The average cycle power P_{QSM}

$$P_{\mathrm{QSM}} = \frac{P_{\mathrm{out}}\, t_{\mathrm{out}} - P_{\mathrm{in}}\, t_{\mathrm{in}}}{t_{\mathrm{total}}} = P_{\mathrm{out}}\, \frac{\dot{l}_{in}}{\dot{l}_{out} + \dot{l}_{in}} - P_{\mathrm{in}}\, \frac{\dot{l}_{out}}{\dot{l}_{out} + \dot{l}_{in}}. \tag{7}$$

can be estimated from the reel-out power ~~P_{opt}~~ P_{out}, the power losses during reel-in P_{in}~~:~~

~~$$P_{\mathrm{QSM}} = P_{\mathrm{out}}\, t_{\mathrm{out}} - P_{\mathrm{in}}\, t_{\mathrm{in}} = P_{\mathrm{out}}\, \frac{\dot{l}_{in}}{\dot{l}_{out} + \dot{l}_{in}} - P_{\mathrm{in}}\, \frac{\dot{l}_{out}}{\dot{l}_{out} + \dot{l}_{in}}.$$~~

, the reel-in time t_{in} and reel-out time t_{out}. We assume reel-in power losses P_{in} to be zero because optimal reel-in tether tension is negligible. This reduces the average cycle power by up to 30%, depending on wind speed. Due to the cyclic nature of the trajectory, we can determine the ratio of the reel-in time t_{in} and reel-out time t_{out} to the total cycle time t_{total} from

the reel-in speed $\dot{l}_{in}$ and reel-out speed $\dot{l}_{out}$. $\dot{l}_{out}$ depends on the wind speed, while the $\dot{l}_{in} = -15\mathrm{ms}^{-1}$ is assumed to be the maximum reel-in speed. ~~We assume a constant~~

During the reel-in and reel-out phases, we assume that the tether force F_{tether} and ~~tether speed during reel-in and reel-out. The transition time between both phases is neglected~~reeling speed remain constant. The time it takes to transition between these two phases is not taken into account. P_{out} is calculated from the product of tether reeling speed $\dot{l}$ and tether tension F_{tether}:

$$P_{\mathrm{out}} = F_{\mathrm{tether}}\,\dot{l}_{\mathrm{out}} = \frac{\rho_{\mathrm{air}}}{2}\frac{\rho}{2} A v U_{\mathrm{app}}^2 c_{\mathrm{R}} \left(\frac{c_{\mathrm{R}}}{c_{\mathrm{D,total}}}\right)^2 \dot{l}_{\mathrm{out}}. \tag{8}$$

Tether tension is a function of ~~wind speed magnitude U~~the apparent wind speed U_{app}, air density ~~ρ_{air}~~ ρ and the resultant aerodynamic force coefficient c_{R} ~~(Equation (3)), which is calculated from the aerodynamic lift c_{L} and total drag coefficient $c_{\mathrm{D,total}}$ (Equation (2)), including wing and tether drag. The tether~~ Equation (3). The apparent wind speed can be nondimensionalized by

$$\frac{U_{\mathrm{app}}}{U(z)} = (\cos\varepsilon\cos\phi - f)\sqrt{1 + \left(\frac{L}{D}\right)^2}. \tag{9}$$

The tether reeling speed $\dot{l}$ is ~~non-dimensionalized in the form~~ nondimensionalized by defining of the reeling factor ~~:~~

$$f = \frac{\dot{l}}{U}, \leq \cos\,\varepsilon\cos\phi\frac{\dot{l}}{U(z)}. \tag{10}$$

~~which is constrained by the~~ The elevation ε and azimuth angle ϕ ~~as~~ constrain $f \leq \cos\varepsilon\cos\phi$ because the magnitude of the apparent wind speed cannot be negative. Combining ~~equation~~ Equations (8) and (10) results in:

$$P_{\mathrm{out}} = \frac{\rho_{\mathrm{air}}}{2}\frac{\rho}{2} A U(z)^3 c_{\mathrm{R}} \left(\frac{c_{\mathrm{R}}}{c_{\mathrm{D,total}}}\right)^2 f\,(\cos\varepsilon\cos\phi - f)^2. \tag{11}$$

The optimal reeling factor ~~is~~ $f_{\mathrm{opt}} = \frac{1}{3}\cos\varepsilon\cos\phi$ ~~which can be derived~~ can be obtained from Equation (11) ~~by a simple~~ through an extreme value analysis. We assume an average reel-out trajectory represented by a single crosswind state instead of tracking the actual trajectory. The trajectory center is aligned with the main wind direction ($\phi = 0°$). The elevation angle ε is determined using the tether length l and operating height z_{oper}. F_{tether} is constrained by the tether diameter d, the tensile strength $\sigma_{\mathrm{max}}^{\mathrm{tether}}$ and the safety factor SF ~~.~~

$$F_{\mathrm{tether}} \leq \frac{d^2}{4}\pi\sigma_{\mathrm{max}}^{\mathrm{tether}}. \tag{12}$$

The power-harvesting factor ζ (Diehl, 2013) is an AWES performance metric.

$$F_{\text{tether}} \leq \frac{d^2}{4}\pi\sigma_{\max}^{\text{tether}}\zeta = \frac{P}{P_{\text{area}}} = \frac{P}{\frac{1}{2}\rho A\overline{U}_{\text{ref}}^3} \tag{13}$$

~~The same sampled WRF-simulated wind profiles (Section 2, Sub-section 2.3) as implemented into the dynamic optimization framework are also investigated using the QSM. We maximize cycle average power P_{QSM} by varying l, $\dot{l}$ and z and assuming optimal $\frac{c_{\text{R}}^3}{c_{\text{D,total}}^2}$. The aircraft is assumed to move directly crosswind with a zero~~ The harvested power P is expressed relative to the kinetic wind energy flow rate P_{area}, P_{area} is a mathematical concept rather than a physical power flux, through an area equivalent to the wing surface area A to nondimensionalize the power. ζ can be derived from Equation (8) by setting the elevation angle ε and the azimuth angle ϕ ~~relative to the wind direction~~to zero.

5.2 WT reference model

This section introduces a ~~simple~~ simplified steady-state ~~WT model to contextualize the AWES performance. WT power is estimated by:~~

reference WT model model that calculates power as

$$P_{\text{WT}} = \frac{1}{2}\rho_{\text{air}}c_{\text{p}}^{\text{WT}}A_{\text{WT}}U^3(z_{\text{WT}} = 100\text{ m}) \tag{14}$$

with a hub height of ~~$z_{\text{WT}} = 100\text{m}$~~ $z_{\text{WT}} = 100$ m for both onshore and offshore conditions. The rotor diameter ~~$D_{\text{WT}} \approx 26.9\text{m}$~~ $D_{\text{WT}} \approx 26.9$ m is sized such that an equivalent rated power of ~~$P_{\text{rated}} = 260\text{kW}$~~ $P_{\text{rated}} = 260$ kW is reached at a rated wind speed of ~~$v_{\text{rated}}(z_{\text{WT}} = 100\text{ m}) = 12\text{ ms}^{-1}$~~ $U_{\text{rated}}(z_{\text{WT}} = 100\text{ m}) = 12\text{ ms}^{-1}$, assuming a constant power coefficient of $c_{\text{p}}^{\text{WT}} = 0.45$. The power is kept constant above the rated wind speed. ~~Performance is compared based on the same sample of~~ The performance of the WT model, dynamic optimization toolbox, and QSM is estimated using the same sampled WRF-simulated wind ~~speed profiles~~conditions (Section 2).

6 Results and discussion

This section analyses the optimization results and compares them to the reference models. ~~Sub-section~~ Subsection 6.1 investigates power-optimal trajectories and the time series of ~~important~~ operational parameters. ~~Sub-section~~ Subsection 6.2 examines operating height statistics, tether length and elevation angle trends. ~~Sub-section 6.3 visualize~~ Subsection 6.3 visualizes the impact of ~~difference~~ wind speeds at different reference heights on ~~a power curveapproximation by comparing average cycle power over $U(z_{\text{ref}} = 100\text{ m})$, $\overline{U}(z_{\text{ref}} = z_{PTH})$ and an apriori guess of the~~ the power curve. We compare three different wind speeds: the wind speed at a reference height of 100 m $\overline{U}_{\text{ref}} = U(z_{\text{ref}} = 100\text{ m})$, the average wind speed at pattern trajectory height $\overline{U}_{\text{ref}} = \overline{U}(z_{\text{ref}} = z_{\text{PTH}})$, and the average wind speed at an a priori guess of pattern trajectory height ~~$\overline{U}(100\text{ m} \leq z_{\text{ref}} \leq 400\text{ m})$. Lastly, Sub-section 6.4 compares the~~ $\overline{U}_{\text{ref}} = \overline{U}(100\text{ m} \leq z_{\text{ref}} \leq 400\text{ m})$. The investigated power curves do not represent design-optimal performance. Subsection 6.4 examines the variation in average cycle power ~~based on simulated WRF wind conditions to~~

~~logarithmic wind speed profiles and contextualizes the data by comparing them to QSM and WT power~~ cased by realistic wind profiles simulated by WRF and compares them to reference power estimates based on logarithmic profiles. All results are subject to the same constraints and design parameters introduced in ~~Section~~ Sections 3 and 4~~and do not represent general ground generation AWES~~.

6.1 Flight trajectory and time series results

Figure 14 compares representative onshore and offshore power-optimal flight trajectories~~subject to a range of illustrative onshore wind conditions~~. These results have been chosen to visualize typical performance optimized trajectories for realistic wind conditions determined with the `awebox`. The reference wind speed ~~mentioned~~ $\overline{U}_{\text{ref}}$ in the legend is the ~~apriori~~ average wind speed at the a priori guess of the pattern trajectory height ~~$U_{\text{ref}} = \overline{U}(100\text{ m} \leq z_{\text{ref}} \leq 400\text{ m})$. These results have been chosen to visualize typical `awebox`-optimized trajectories derived from realistic wind conditions.~~ $z_{\text{ref}}(100\text{ m} \leq z_{\text{ref}} \leq 400\text{ m})$.

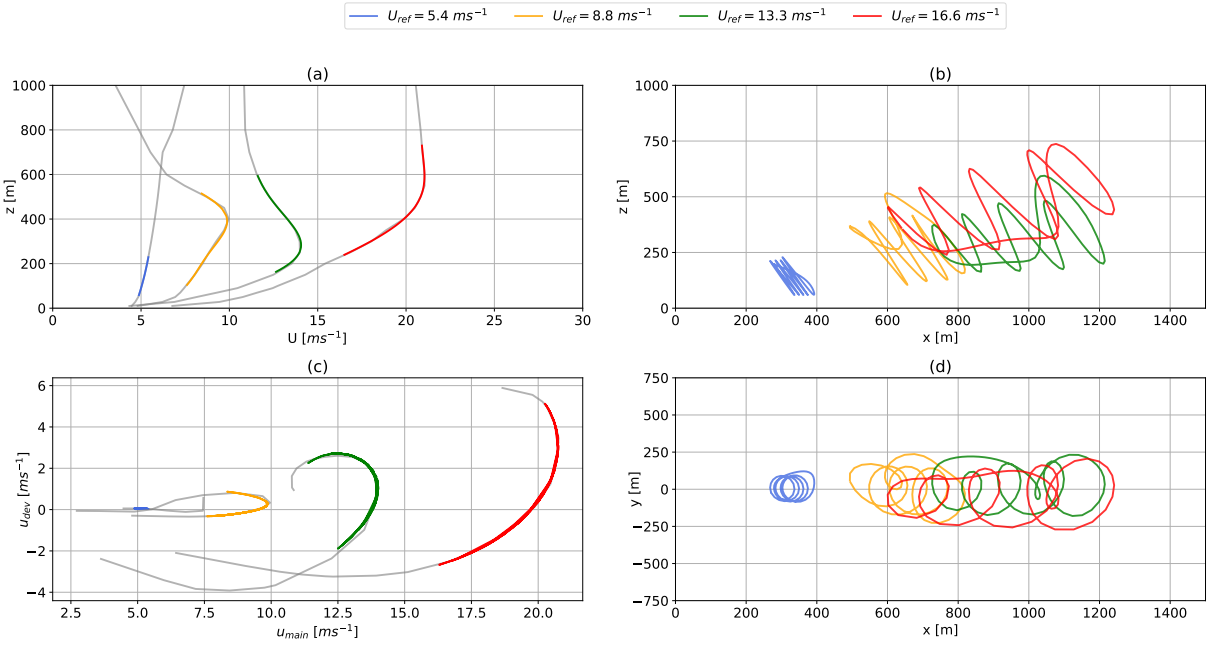

Figure 14. ~~Exemplary onshore trajectories. Wind data are based on sampled~~ Representative WRF-simulated ~~clusters (Section 2). Wind~~ vertical onshore wind speed ~~magnitude~~ profiles U (a), and hodograph (top view) ~~of wind velocity~~ up to 1000 m (c). The highlighted sections indicate ~~operating~~ Lagrangian polynomial fit of the wind ~~conditions~~velocity at operating height. Panel (b) and panel (d) ~~shows~~ show the side and top view of the corresponding `awebox`-optimized trajectories. The reference wind speed in the legend is ~~$U_{\text{ref}} = \overline{U}(100\text{ m} \leq z_{\text{ref}} \leq 400\text{ m})$~~$\overline{U}_{\text{ref}} = \overline{U}(100\text{ m} \leq z_{\text{ref}} \leq 400\text{ m})$. The results correspond to the time series shown in Figure 16.

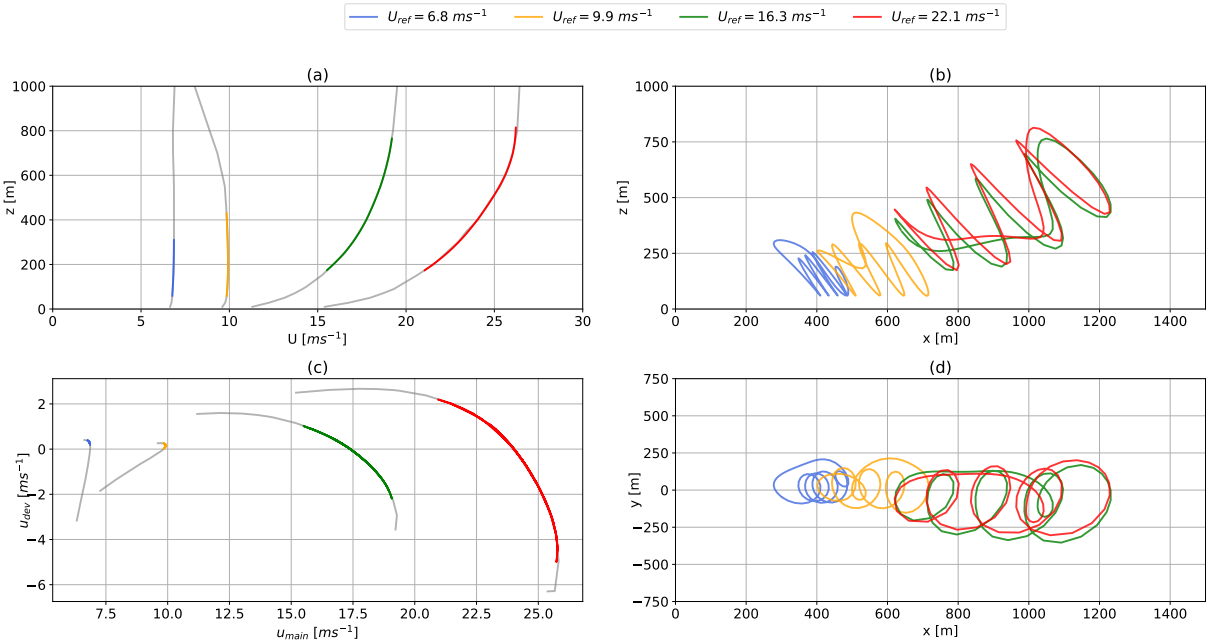

Figure 15. Representative WRF-simulated vertical offshore wind speed profiles U (a), and hodograph (top view) up to 1000 m (c). The highlighted sections indicate Lagrangian polynomial fit of the wind velocity at operating height. Panel (b) and panel (d) show the side and top view of the corresponding awebox-optimized trajectories. The reference wind speed in the legend is $\overline{U}_{\text{ref}} = \overline{U}(100\ \text{m} \leq z_{\text{ref}} \leq 400\ \text{m})$. The results correspond to the time series shown in Figure 17.

Figure 14 (a) shows the ~~wind speed magnitude~~ magnitude of the vertical wind velocity profile U ~~over altitude z~~. Figure 14 (c) shows the corresponding top view of the wind velocity ~~profiles~~profile, rotated such that ~~u_{main}~~ the main wind component (average wind direction between 100 m and 400 m) u points in positive x direction. The WRF-simulated wind profiles are shown in gray. The highlighted segments depict the Lagrangian polynomial fit (Abramowitz and Stegun, 1965) at operating heights~~, which sufficiently fits the~~ . These polynomials that have been incorporated into the optimization toolbox provide a sufficient fit for the wind data. Figures 14 (b) and (d) show a side ($x-z$ plane) and top view ($x-y$ plane) of the optimized trajectories. The optimization predicts an increase in tether length, operating height and stroke length with wind speed. ~~Similar~~ Figure 15 shows similar results for the offshore location~~can be found in Figure 15 in the appendix.~~

. Figure 16 illustrates the corresponding temporal development of important operational parameters.

The optimizer maximizes tether tension by adjusting the reel-out speed and angle of attack (Figure 16 (a)) during reel-out even for lower wind speed and adjusts the reel-out speed (Figure 16 (c)) to maximize average cycle power. This ~~increases~~ causes the reeling factor ~~beyond its optimal~~ to exceed its optimal value of $f_{\text{opt}} = \frac{1}{3}\cos\varepsilon\cos\phi$ ~~and increases power with wind speed even though the maximum tether force is reached. The resulting instantaneous power is shown in~~ at high wind speeds, resulting

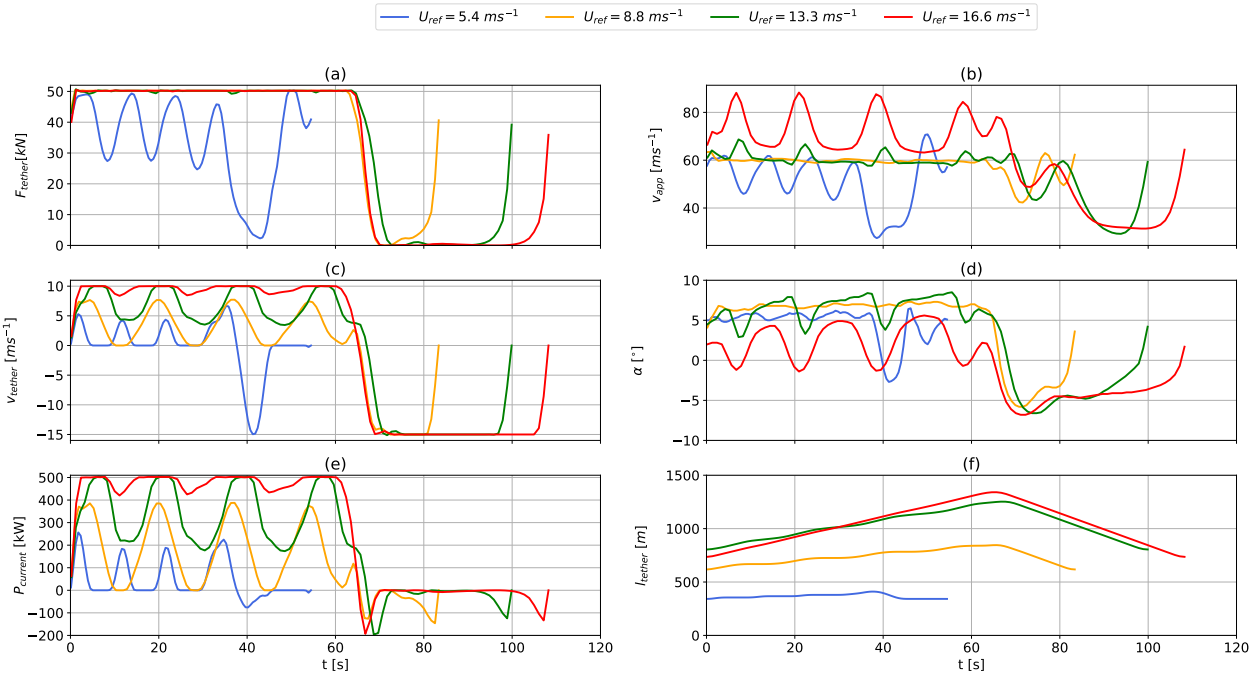

Figure 16. Time series of instantaneous tether tension (a), apparent wind speed (b), tether-reeling speed (c), angle of attack ~~a~~ (d), power output (e) and tether length (f) ~~. The results correspond to the trajectories,~~ over one pumping based on ~~sampled~~ representative onshore WRF-simulated wind data~~,~~. The results correspond to trajectories shown in Figure 14.

in an increase in power (Figure 16 (e)) even when the maximum tether force has been reached. The low wind speed example ~~$U_{\text{ref}} = 5.4\text{ms}^{-1}$~~ $\overline{U}_{\text{ref}} = 5.4\ \text{ms}^{-1}$ (blue) seems to be just above cut-in wind speeds. ~~Its tether speed drops~~ The tether reeling speed decreases to zero for ~~an extended amount of time~~ a prolonged period during the reel-out phase ~~to maintain sufficient~~ in order to generate enough lift to keep the aircraft aloft. The production period remains almost constant (~~$t \approx 60sec$~~ ≈ 60 sec) for the moderate and high wind speed trajectories (orange, green and red), while the reel-in period increases with wind speed, due to the increased reel-out length caused by a higher average reel-out speed. ~~Significant power losses only occur~~ There are significant power losses during the transition between the production and retraction ~~phase~~phases when the tether is being reeled in and the tension remains high because the aircraft is unable to depower quickly enough. During the reel-in phase, the tether reeling speed reaches its limit while the tether tension decreases to zero as the ~~tether speed is maxed out while tether tension drops to zero and the~~ aircraft reduces its angle of attack and lift (Figure 16 (d))~~to reduce lift~~. At higher wind speeds the optimizer ~~extends the trajectories perpendicular to the main wind direction,~~ increases the elevation angle and reduces angle of attack to stay within the constraints. This can ~~results~~ result in odd or unexpected trajectories, even though these local minima are feasible solutions within the system constraints. Tether length (Figure 16 (f)) generally increases with wind speed as the

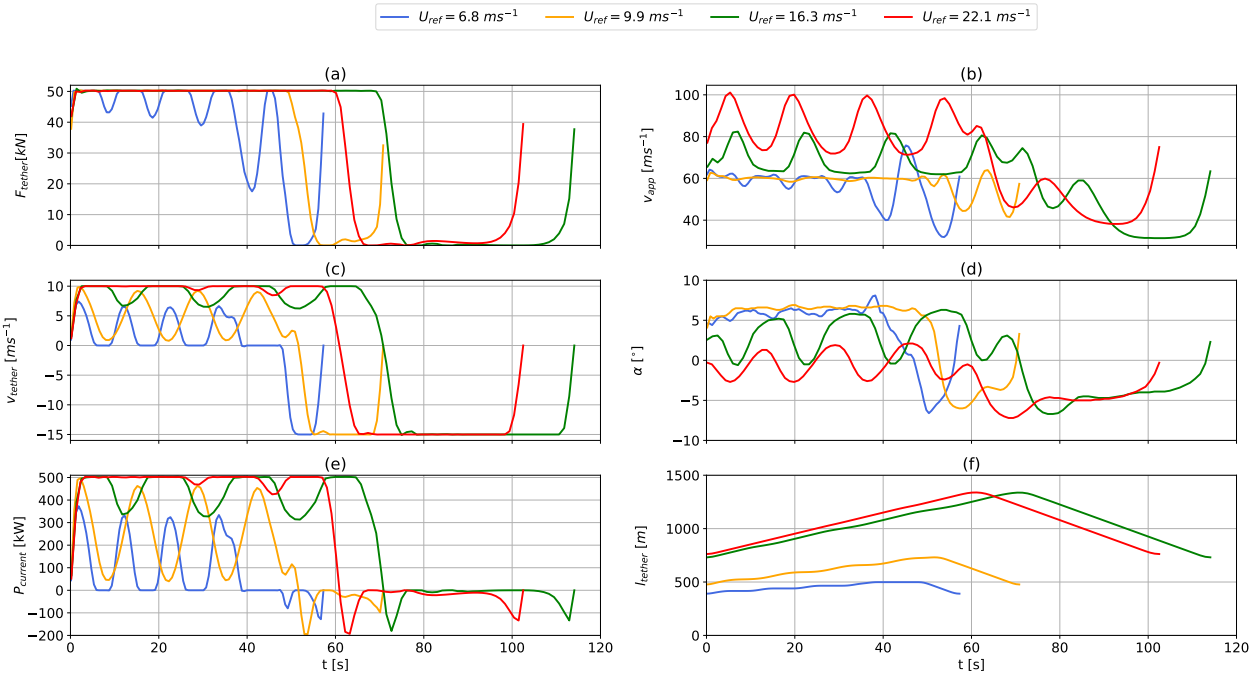

Figure 17. Time series of instantaneous tether tension (a), apparent wind speed (b), tether-reeling speed (c), angle of attack (d), power output (e) and tether length (f) over one pumping based on representative offshore offshore WRF-simulated wind data. The results correspond to trajectories shown in Figure 15.

system reels out faster, increases its elevation angle and operates at higher altitude. Similar results for the offshore location ~~can be found~~ are shown in Figure 17~~in the appendix~~.

6.2 Tether length, elevation angle and operating altitude

~~This sub-section compares tether lengths l, elevation angles ε and operating heights $z_{\text{operating}}$ resulting from the trajectory optimization of 60 wind velocity profiles from $k = 20$ clusters.~~ Figure 18 (a) illustrates the range of tether lengths l for each of the 60 onshore (blue) and offshore (orange) ~~tether lengths l of each wind velocity profile~~wind velocity profiles. The maxima and minima are highlighted by circles and plotted over reference wind speed $\overline{U}(z_{\text{ref}} = 100 - 400\ \text{m})$.

None of the optimizations ~~max out the~~ reach the maximum tether length constraint of ~~$l^{\max} = 2000$ m~~$l_{\max} = 2000$ m because a longer tether would not be advantageous due to the added drag and weight, which would decrease performance. Both locations show a trend towards longer ~~tether lengths~~ tethers up to rated wind speed, where the reel-out speed and tension are almost constant and close to ~~maximum~~ their respective constraint (Figure 16). ~~A longer tether is not beneficial as the AWES needs to stay within design constraints and the additional drag and weight would only reduce performance.~~ The maximum tether length remains almost constant above rated wind speed while the minimum tether length increases slightly, reducing the total stroke

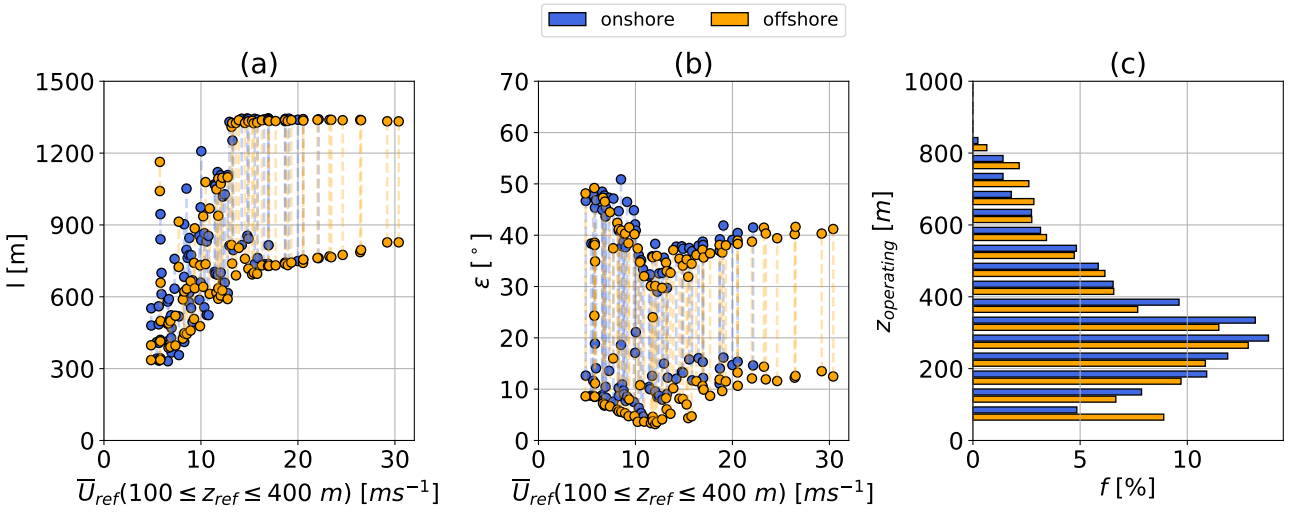

Figure 18. Tether length range (a) ~~over reference wind speed $U(z_{\mathrm{ref}} = 100 - 400\ \mathrm{m})$~~ and frequency distribution of operating ~~altitude~~ height z_{oper} (b) over reference wind speed $U(z_{\mathrm{ref}} = 100 - 400\ \mathrm{m})$ based on `awebox` trajectory ~~optimization of k~~ optimizations of k = 20 onshore (blue) and offshore (orange) clusters.

length. The elevation angle (Figure 18 (b)) decreases as the tether length increases. The optimizer tries to keep the elevation angle low in order to reduce misalignment (cosine) losses between the tether and the ~~horizontal~~ wind velocity vector. The onshore elevation angle is slightly higher ~~due to the higher wind shearwhich justifies~~ because of the increased wind shear, which makes higher operating altitudes more justifiable. This can also be seen in Figure 18 (c) which shows the frequency distribution of operating altitude~~$z_{\mathrm{operating}}$~~. Of the optimal operating heights, 78.6% onshore and 74.7% offshore ~~the optimal operating heights~~ are below 400 ~~m~~meters, confirming the findings in Sommerfeld et al. (2019a, b). Larger or ~~multi-kite~~ multikite AWES could benefit from higher operating altitudes due to their higher lift to tether drag ratio and lift to tether weight ratio, but more detailed analyses are required.

6.3 Impact of reference height on power curve

The power curve of wind energy converters ~~depicts the average power over~~ quantifies the power that can be harvested at a given reference wind speed. For conventional ~~WT~~ WTs the wind speed at hub-height is commonly used as reference wind speed. Whether this is appropriate for ever growing towers ~~an longer WT~~ and longer rotor blades is debatable (???). Defining a reference wind speed for AWES is not trivial, as ~~they change their operating height with wind speed, during each cycle and dependent on~~ the operating height dependents on the shape and magnitude of the vertical wind speed profile~~shape~~. The choice of reference wind speed impacts the power curve representation. The AWE Glossary (Airborne Wind Europe, 2021) recommends to use the wind speed at pattern trajectory height z_{PTH}, which is the expected or logged time-averaged height during the power production phase, as reference wind speed. We estimate $100\ \mathrm{m} \leq z_{\mathrm{ref}} \leq 400\ \mathrm{m}$ as an ~~apriori~~ a priori guess

of the ~~wind speed at~~ pattern trajectory height. ~~We do not claim to define a general power curve, but rather investigate the variaton of average cycle power caused by realistic wind profiles.~~ Figure 19 compares onshore (a) and offshore (b) average cycle power over $U(z_{\mathrm{ref}} = 100\ \mathrm{m})$ (blue), ~~$\overline{U}(z_{\mathrm{ref}} = z_{PTH})$~~ $\overline{U}(z_{\mathrm{ref}} = z_{\mathrm{PTH}})$ (green) and an ~~apriori~~ a priori guess of the wind speed at pattern trajectory height $\overline{U}(100\ \mathrm{m} \leq z_{\mathrm{ref}} \leq 400\ \mathrm{m})$ (orange).

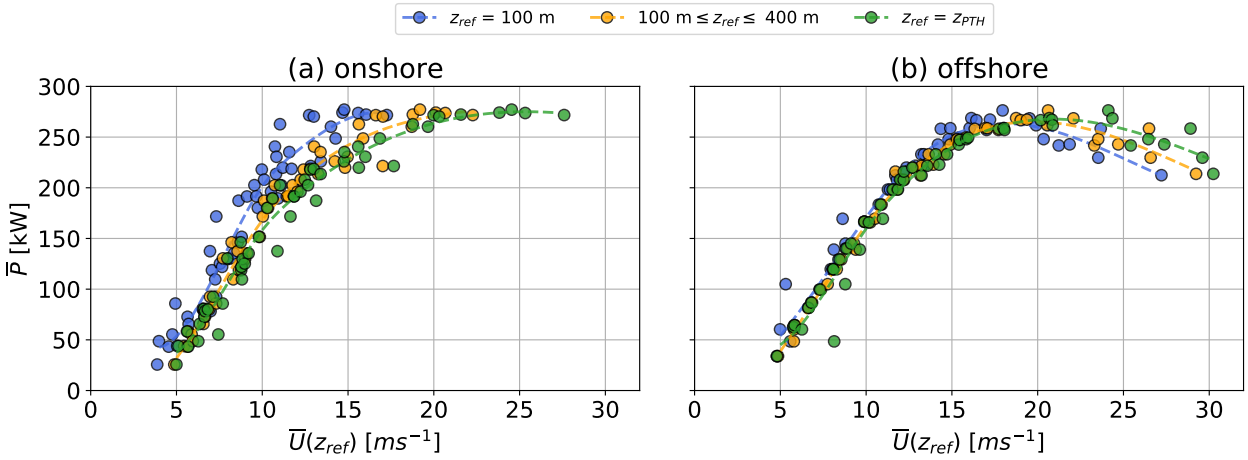

Figure 19. Onshore (a) and offshore (b) AWES power curve approximations ~~over~~ with wind ~~speed~~ speeds at $z_{\mathrm{ref}} = 100$ m (blue), $100\ \mathrm{m} \leq z_{\mathrm{ref}} \leq 400$ m (orange) and $z_{\mathrm{ref}} = z_{\mathrm{PTH}}$ (green) reference ~~height~~heights. The dashed lines ~~are~~ represent least-square spline ~~interpolation with a knot at $U_{\mathrm{ref}} = 13\ \mathrm{ms}^{-1}$~~interpolations that have been added to aid in visualization.

~~The data points correspond to the clustered and~~ Each data point corresponds to one of the sampled WRF-simulated wind ~~speed profiles~~ velocity profiles U. The dashed lines, which are only added as visual aid, are a least-square spline interpolation of the approximately 60 data points~~with a knot at $U_{\mathrm{ref}} = 12\ \mathrm{ms}^{-1}$. This spline definition is chosen to account for the difference in power up to and above rated wind speed.~~

~~The choice of~~ . Based on these results, we can conclude that the selection of the reference height is more ~~significant onshore~~ important for onshore conditions. The onshore wind conditions with their higher number of non-monotonic wind ~~speed~~ profiles and higher wind shear lead to ~~more fluctuation~~ larger deviations from the typical power curve shape described in (Licitra et al., 2019; Airborne Wind Europe, 2021) and others. The higher wind shear onshore leads to a shift towards lower wind speeds for a reference height of $z_{\mathrm{ref}} = 100$ m. The ~~apriori~~ a priori pattern trajectory height guess of $100\ \mathrm{m} \leq z_{\mathrm{ref}} \leq 400\ \mathrm{m}$ is relatively close to the actual z_{PTH}, especially for lower wind speeds. At very high wind speeds above ~~$\overline{U}_{\mathrm{ref}} \geq 20\mathrm{ms}^{-1}$~~ $\overline{U}_{\mathrm{ref}} \geq 20\ \mathrm{ms}^{-1}$ the z_{PTH} power shifts towards higher wind speeds indicating ~~a higher operating altitude~~an increased operating height.

The more homogeneous offshore wind conditions result in less power variation. The three different reference heights have almost no impact on the offshore power curve up to the rated wind speed. Above ~~$\overline{U}_{\mathrm{ref}} \geq 20\mathrm{ms}^{-1}$~~ $\overline{U}_{\mathrm{ref}} \geq 20\ \mathrm{ms}^{-1}$ the power curves diverge and the average cycle power decreases. This seems to be a result of the `awebox` optimization and its initializa-

tion with a fixed number of ~~loops~~loop maneuvers. As the wind speed and reel-out speed increase, the aircraft cannot complete all the ~~loops~~ loop maneuvers before reaching the maximum tether length and transitioning into reel-in. Therefore, one of the ~~loops is performed during the reel-in~~loop maneuvers is performed when already reeling in, leading to an increase in tether tension (Figure A1 (a)) and additional losses during the reel-in period (Figure A1 (e)). The corresponding trajectories are shown in Figure A2 in the appendix.

~~Time series of instantaneous tether tension (a), apparent wind speed (b), tether-reeling speed (c), angle of attack α (d), power (e) and tether length (f) for high speed WRF-simulated offshore wind conditions. The results correspond to the trajectories shown in Figure A2.~~

6.4 Reference model power comparison

Figure 20 ~~presents the impact of the wind speed profile shape on optimized average cycle power $\overline{P}$ over~~ compares the variation in the power curve for a refernce wind speed of $\overline{U}_{\text{ref}}(100\text{ m} \leq z_{\text{ref}} \leq 400\text{ m})$ ~~, by comparing power estimates~~ based on sampled WRF-simulated wind data (blue) ~~to~~ and power estimates based on standard logarithmic wind speed profiles (red). These results are verified against the QSM (~~Sub-section~~ Subsection 5.1, orange) and WT reference models (~~Sub-section~~ Subsection 5.2, green).

The QSM and WT reference model use the same sampled WRF-simulated wind data. No cut-out wind speed is defined. The cut-in wind speed of $\overline{U}_{\text{ref}} \approx 5\ \text{ms}^{-1}$ is the result of unconverged optimizations~~below this threshold~~. The optimization algorithm was not able to find a feasible trajectory for these low wind speeds, indicating that the wind is insufficient to keep the AWES aloft and produce power. The QSM and WT model estimate power for these wind speeds. Rated power is achieved around ~~$U_{\text{rated}} \approx 12 - 15\text{ms}^{-1}$~~$U_{\text{rated}} \approx 12 - 15\ \text{ms}^{-1}$, depending on the wind speed profile shape. At ~~this wind speed~~ these wind speeds the reel-out speed is almost constant while a constant reel-out tension is already achieved at lower wind speeds (Figure 16).

The logarithmic wind speed profiles (Equation (6)) use ~~a~~ roughness lengths of $z_0^{\text{onshore}} = 0.1$ and $z_0^{\text{offshore}} = 0.001$. Onshore, the power predicted based on WRF wind data is often higher than the power predicted using logarithmic profiles (~~Sub-section 4.4). As expected, logarithmic power estimates do not fluctuate as much as the WRF-simulated power . The predicted logarithmic onshore power (~~Figure 20 (a))~~is often slightly below WRF which could indicate that these WRF profiles exhibit narrow areas of higher wind speeds, such as LLJs~~ . This is likely due to higher than predicted wind shear and the presence of LLJs that are not represented by logarithmic profiles. Offshore, the logarithmic and WRF data are in ~~good~~ close agreement with the logarithmic results ~~as~~ because most of the simulated wind profiles are more monotonic. ~~At both locations, the higher WRF power above $U_{\text{ref}} \geq 15\ \text{ms}^{-1}$ is likely caused by higher than logarithmic wind shear. However, another contributing factor is the `awebox` optimization and initialization with a fixed number of loops which can lead to loops being performed during the reel-in period which leads to a reduction in average cycle power. Additionally, determining a dynamically feasible and power-optimal trajectory becomes more difficult at higher wind speeds, due to tether speed and tension constraints.~~

The ~~power-harvesting factor ζ (Diehl, 2013) is an AWES performance indicator. It expresses the estimated AWES power P relative to the total wind power P_{area} through an area of the same size as the wing A. Here the average wind speed~~

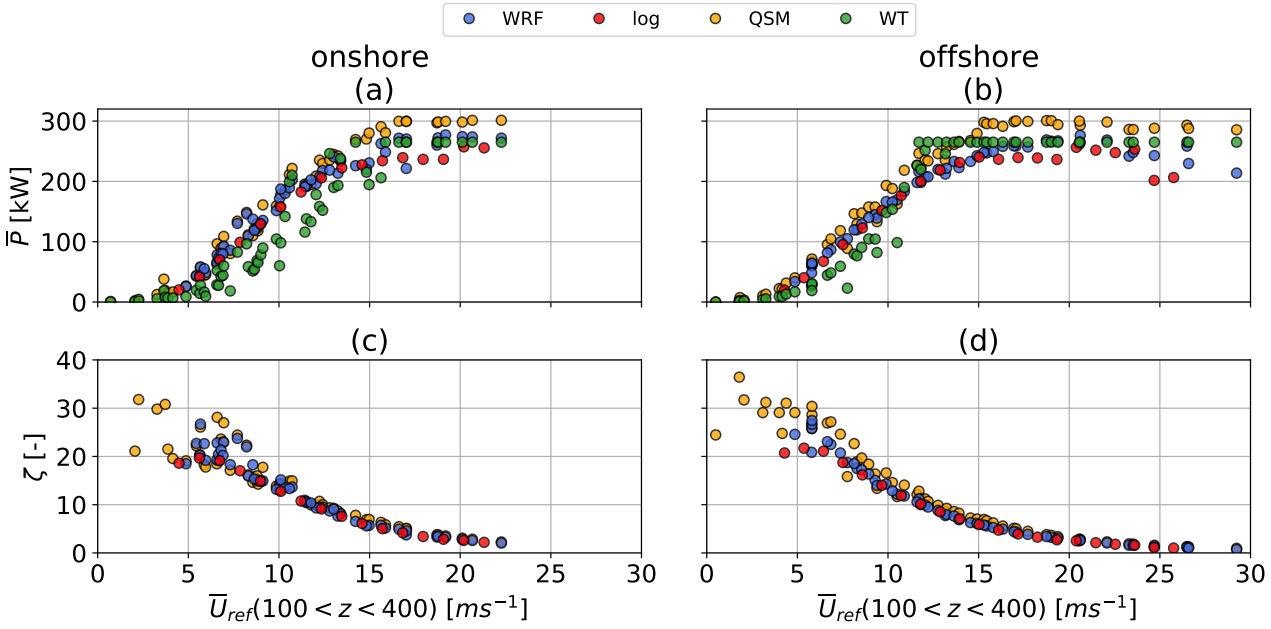

Figure 20. ~~Onshore~~ Average cycle power $\overline{P}$ and power-harvesting factor ζ for the onshore (a, c) and offshore (b, d) location as a function of average ~~cycle power $\overline{P}$ over average~~ wind speed $\overline{U}_{\text{ref}}$ between 100 and 400 meters. ~~WRF~~ The data points obtained from awebox (blue)~~data~~, QSM (orange), and the WT model (green) are based on ~~3~~ WRF wind ~~speed profiles for each of the $k = 20$ clusters, is~~ data and are compared to awebox data derived from standard logarithmic wind speed profiles (red). ~~QSM (orange) and WT (green) which use the same sampled WRF profiles are added for reference. The onshore (c) and offshore (d) power-harvesting factor ζ is added as an performance indicator.~~

~~between $\overline{U}_{\text{ref}}(100 \leq z_{\text{ref}} \leq 400\ \text{m})$ is use to calculate P_{area}, which is not a physical power, but a mathematical concept to non-dimensionalize power.~~

$$\zeta = \frac{P}{P_{\text{area}}} = \frac{P}{\frac{1}{2}\rho_{\text{air}} A U_{\text{ref}}^3}$$

~~ζ can be derived from (8) by setting the elevation angle ε and the azimuth angle ϕ to zero. An extreme value analysis results in an optimal reel-out speed $\dot{l} = 1/3\ U$ (Equation (10)) and $\zeta_{\max} = \frac{4}{27} c_{\text{R}} \left(\frac{c_{\text{R}}}{c_{\text{D}}}\right)^2$.~~

~~Both~~ trends for both onshore (Figure 20 (c)) and offshore (Figure 20 (d)) ~~show similar trends in agreement with the QSM. ζ decreases with wind speed because tether tension and speed constraints need to be satisfied. Both the QSMand WT reference model use the same sampled WRF-simulated wind data~~conditions show a decrease with increasing wind speed and are consistent with the QSM. WT power fluctuates ~~significantly~~ due to the choice of reference height. AWESs outperform WTs up to rated wind speed, particularly onshore where AWESs can take advantage of higher wind speeds aloft. Lower wind shear offshore reduces the need to operate at higher altitudes, reducing the benefit of AWESs. ~~As expected, the~~ The QSM predicts

the highest power~~due to the simplified model and~~ , as anticipated, due to its simplified assumptions such as constant power during reel-out and reel-in ~~power~~ and neglected mass.

7 Conclusions and outlook

This ~~study describes optimal~~ research outlines the optimal performance of single-aircraft, ~~ground generation AWES performance based on~~ ground-generation AWES using sampled mesoscale WRF-simulated wind data ~~by analyzing~~ and compares it to the average cycle power calculated using standard logarithmic wind profiles. It also describes trajectories, instantaneous performance, ~~operating heights and average cycle power. Throughout the paper an apriori operating heights guess of $100 \leq z_{\mathrm{ref}} \leq 400$ m is used. This guess is verified by comparing the power curve approximations over wind speed at different reference heights.~~ and trends in tether length and operating height. These analyses use one year of onshore wind data at Pritzwalk in northern Germany and one year of offshore wind data at the FINO3 research platform in the North Sea to drive the `awebox` optimization~~framework~~, which determines dynamically feasible, power-optimal trajectories. The ~~model uses a scaled Ampyx AP2 aircraft with a wing area of $A = 20$ m^2 and is subject to realistic constraints. The~~ annual wind data ~~set~~ is categorized into ~~k~~ k = 20 clusters ~~using k-means~~ of vertical wind velocity profiles $\mathbf{U}$ using a k-means clustering algorithm. To ~~reduce the computational cost, only three wind speed profiles per cluster are implemented into the optimization model. These profiles are sampled~~ decrease the computational expense, three profiles based on the 5th, 50th, and 95th percentile of wind speed between $\overline{U}_{\mathrm{ref}}(100 \leq z_{\mathrm{ref}} \leq 400\ \mathrm{m})$ ~~to represent the in-cluster variation~~for each cluster are incorporated into the performance optimization model. The performance model uses a scaled Ampyx Power AP2 aircraft with a wing surface area of $A = 20$ m^2 and is subject to realistic tether and operational constraints. Our investigation into the impact of wind speed at reference height found that the a priori guess of $100 \leq z \leq 400$ m is a good guess for the investigated AWES design and size. Optimal average cycle power is compared to a quasi-steady-state AWES model and a steady-state WT model.

The optimization model is able to determine power-optimal trajectories for complex, non-monotonic wind ~~speed~~ velocity profiles. The optimized results are only ~~slightly lower than the QSM predictions, which assume constant reel-out power, no~~ marginally lower than those obtained using the simplified QSM, which neglects the effects of gravity and only simulates a single reel-in ~~power losses and neglect gravity~~and reel-out state instead of the entire trajectory. The predicted onshore AWES power exceeds the WT reference model~~onshore because it can utilize the~~ . This is because AWES can adapt their operating altitude to benefit from higher wind shear ~~and can operate at high wind speed altitudes such as LLJ noses. These conditions are not represented by simple logarithmic wind speed profiles which is why average power is generally lower than for WRF-simulated wind. Offshore wind conditions, which are~~ or LLJs. Offshore wind velocity profiles are generally more monotonic and ~~have less wind shear, produce similar average power as~~ exhibit higher wind speeds, with less turbulence and wind shear. As a result, offshore winds produce average power that is similar to their logarithmic approximation. Due to the initialization of the `awebox` with a fixed number of ~~loops,~~ loop maneuvers, which is not a variable in the objective function, high wind speed trajectories show loops during the reel-in period which reduces the average cycle power. ~~The number of loops is currently not~~

~~a variable in the objective function of the awebox.~~ This can lead to a deterioration of the trajectory at high wind speeds, as the optimizer struggles to stay within the tether tension and tether reeling speed constraint.

An investigation of the ~~instantaneous performance shows~~ time series data show that the optimizer first maximizes tether tension ~~and adjusts~~ by adjusting reel-out speed and angle of attack. With increasing wind speed the tether reel-out speed ~~becomes more constant and~~ approaches the maximum reel-out speed ~~constraint~~limit and steadier. Up to rated wind speed, when average tether tension and tether reeling speed are maximized, the optimizer increases the deployed tether length and reduces the elevation angle to operate at optimal height. At higher wind speeds, the elevation angle increases to de-power the system and stay within design constraints. As a result, approximately 75% of the optimal onshore and offshore operating heights are below 400 m. ~~This informs airspace regulators and companies to address airspace restriction challenge and weakens the claim in some early airborne wind energy literature of increased power harvest way above 500 m. The onshore power curve estimation, using the average wind speed between $100 \leq z_{\text{ref}} \leq 400$ m as reference wind speed, slightly overestimates power in comparison to the wind speed at pattern trajectory height, which is the expected or actual time-averaged height during the reel-out (power production) phase. Offshore, the power curve seems independent of~~ The offshore power curve appears to be independent of the reference height due to the lower number of non-monotonic wind speed profiles and lower wind shear. In contrast, the choice of reference height is more important for the onshore power curve.

The mesoscale wind simulations, which ~~comprise of 1 year~~include a year's worth of wind data with a temporal resolution of 10 minutes~~at both locations, are categorized and analyzed~~, are analyzed and categorized for both onshore and offshore locations. The annual wind roses for heights of 100 and 500 m confirm the expected wind speed increase and clockwise rotation at both locations. Offshore shows a lower wind shear and veer than onshore. Annual wind speed statistics reveal that low wind speeds still occur at a fairly high probability up to 1000 m at both locations. The ~~*k*-means~~ k-means clustering algorithm is able to categorize the wind regime and identify LLJs as well as various non-logarithmic and non-monotonic wind profiles. The ~~main deciding factor seems to be the~~ primary factor in assigning a profile to a cluster appears to be wind speed, while the ~~profile shape seems to play a less important role~~shape of the profile seems to have a lesser impact. Individual clusters produce coherent groups of similar wind profiles whose probability correlates with seasonal, diurnal and atmospheric stability variation. ~~*k*-means clustering~~ The k-means clustering method provides good insight into the wind regime, especially for higher altitudes where classification by Obukhov length is inadequate.

~~A~~ As a continuation of this ~~research includes the derivation of AEP based on~~ study, the power curves and realistic wind conditions ~~.~~ described here could be utilized to calculate AEP estimations. Further research is required into AWES power curves and their reference wind speed~~also needs to be investigated further, for example by comparing~~ , which could be accomplished by deriving shape-specific power curves from normalized wind speed profiles or ~~including~~ by considering the correlation between wind speeds at different reference heights. Future work ~~could analyze the impact of different number of initialization loops or include the number of loops in the objective function of the optimization~~should include a variable number of loop maneuvers as a variable in the optimization objective function. Using the same data and model, it is possible to investigate the annual and diurnal AWES power variation in comparison to WT performance. A parallel sizing study ~~(Sommerfeld et al., 2020)~~ (**?**) using the same wind clustered wind data ~~investigates~~ investigated the impact of mass and aerodynamic efficiency on AWES

performance. Adding a design optimization to the awebox model ~~enables~~ could enable location-specific aircraft and tether investigation.

7.1 Acknowledgments and funding sources

The authors thank the BMWi for the funding of the "OnKites I" and "OnKites II" projects [grant numbers 0325394 and 0325394A] on the basis of a decision by the German Bundestag and project management Projektträger Jülich. We thank the PICS, NSERC and the DAAD for their funding.

awebox has been developed in collaboration with the company Kiteswarms Ltd. The company has also supported the awebox project through research funding. The awebox project has received funding from the European Union's Horizon 2020 research and innovation program under the Marie Sklodowska-Curie grant agreement no. 642682 (AWESCO).

We thank the Carl von Ossietzky University of Oldenburg and the Energy Meteorology research group for providing access to their high performance computing cluster *EDDY* and ongoing support.

We further acknowledge Rachel Leuthold (University of Freiburg, SYSCOP) and Thilo Bronnenmeyer (Kiteswarms Ltd.) for their help in writing this article, great, technical support and continued work on the awebox toolbox.

7.2 Author contribution

Markus Sommerfeld evaluated the data and wrote the manuscript in consultation with and under the supervision of Curran Crawford. Martin Dörenkämper set up the numerical offshore simulation and contributed to the meteorological evaluation of the data and reviewed the manuscript. Jochem De Schutter co-developed the optimization model and helped to write and ~~reviewe~~ review this manuscript.

References

EnerKíte - Technologie, http://www.enerkite.de/technologie, 2016.

Abramowitz, M. and Stegun, I. A., eds.: Handbook of Mathematical Functions with Formulas, Graphs and Mathematical Tables, Dover Publications, Inc., New York, 1965.

Airborne Wind Europe: Airborne Wind Energy Glossary, https://airbornewindeurope.org/resources/glossary-2/, last accessed: 2022-03-29, 2021.

Ampyx: Ampyx Power BV, https://www.ampyxpower.com/, 2020.

Archer, C. L., Colle, B. A., Veron, D. L., Veron, F., and Sienkiewicz, M. J.: On the predominance of unstable atmospheric conditions in the marine boundary layer offshore of the U.S. northeastern coast, Journal of Geophysical Research: Atmospheres, 121, 8869–8885, https://doi.org/10.1002/2016JD024896, 2016.

Argatov, I. and Silvennoinen, R.: Efficiency of Traction Power Conversion Based on Crosswind Motion, in: Airborne Wind Energy, edited by Ahrens, U., Diehl, M., and Schmehl, R., pp. 65–79, Springer, Berlin, Heidelberg, https://doi.org/10.1007/978-3-642-39965-7_4, 2013.

Argatov, I., Rautakorpi, P., and Silvennoinen, R.: Estimation of the mechanical energy output of the kite wind generator, Renewable Energy, 34, 1525–1532, https://doi.org/10.1016/j.renene.2008.11.001, 2009.

Arya, P. and Holton, J.: Introduction to Micrometeorology, International Geophysics, Elsevier Science, 2001.

Aull, M., Stough, A., and Cohen, K.: Design Optimization and Sizing for Fly-Gen Airborne Wind Energy Systems, Automation, 1, 1–16, https://doi.org/10.3390/automation1010001, 2020.

Banta, R. M.: Stable-boundary-layer regimes from the perspective of the low-level jet, Acta Geophysica, 56, 58–87, https://doi.org/10.2478/s11600-007-0049-8, 2008.

Bechtle, P., Schelbergen, M., Schmehl, R., Zillmann, U., and Watson, S.: Airborne wind energy resource analysis, Renewable Energy, 141, 1103 – 1116, https://doi.org/https://doi.org/10.1016/j.renene.2019.03.118, 2019.

Bronnenmeyer, T.: Optimal Control for Multi-Kite Emergency Trajectories, Master's thesis, University of Stuttgart, https://cdn.syscop.de/publications/Bronnenmeyer2018.pdf, last accessed: 2022-11-09, 2018.

Carl von Ossietzky Universität Oldenburg: EDDY @ONLINE, https://www.uni-oldenburg.de/fk5/wr/hochleistungsrechnen/hpc-facilities/eddy/, 2018.

Cherubini, A., Papini, A., Vertechy, R., and Fontana, M.: Airborne Wind Energy Systems: A review of the technologies, Renewable and Sustainable Energy Reviews, 51, 1461–1476, https://doi.org/10.1016/j.rser.2015.07.053, 2015.

De Schutter, J., Leuthold, R., Bronnenmeyer, T., Paelinck, R., and Diehl, M.: Optimal control of stacked multi-kite systems for utility-scale airborne wind energy, in: 2019 IEEE 58th Conference on Decision and Control (CDC), pp. 4865–4870, https://doi.org/10.1109/CDC40024.2019.9030026, 2019.

De Schutter, J., Malz, E., Leuthold, R., Bronnenmeyer, T., Paelinck, R., and Diehl, M.: `awebox`: Modelling and optimal control of single- and multiple-kite systems for airborne wind energy, https://github.com/awebox, last accessed: 2021-10-11, 2020.

Dee, D. P., Uppala, S. M., Simmons, A. J., Berrisford, P., Poli, P., Kobayashi, S., Andrae, U., Balmaseda, M. A., Balsamo, G., Bauer, P., Bechtold, P., Beljaars, A. C. M., van de Berg, L., Bidlot, J., Bormann, N., Delsol, C., Dragani, R., Fuentes, M., Geer, A. J., Haimberger, L., Healy, S. B., Hersbach, H., Hólm, E. V., Isaksen, L., Kållberg, P., Köhler, M., Matricardi, M., McNally, A. P., Monge-Sanz, B. M., Morcrette, J.-J., Park, B.-K., Peubey, C., de Rosnay, P., Tavolato, C., Thépaut, J.-N., and Vitart, F.: The ERA-Interim reanalysis:

configuration and performance of the data assimilation system, Quarterly Journal of the Royal Meteorological Society, 137, 553–597, https://doi.org/10.1002/qj.828, 2011.

Diehl, M.: Airborne Wind Energy: Basic Concepts and Physical Foundations, in: Airborne Wind Energy, edited by Ahrens, U., Diehl, M., and Schmehl, R., pp. 3–22, Springer, https://doi.org/10.1007/978-3-642-39965-7_1, 2013.

Donlon, C. J., Martin, M., Stark, J., Roberts-Jones, J., Fiedler, E., and Wimmer, W.: The Operational Sea Surface Temperature and Sea Ice Analysis (OSTIA) system, Remote Sensing of Environment, 116, 140–158, https://doi.org/10.1016/j.rse.2010.10.017, 2012.

Dörenkämper, M., Optis, M., Monahan, A., and Steinfeld, G.: On the Offshore advection of Boundary-Layer Structures and the Influence on Offshore Wind Conditions, Boundary-Layer Meteorol., 155, 459–482, https://doi.org/10.1007/s10546-015-0008-x, 2015.

Dörenkämper, M., Stoevesandt, B., and Heinemann, D.: Derivation of an offshore wind index for the German bight from high-resolution mesoscale simulation data, Proceedings of DEWEK - German Offshore Wind Energy Conference, p. 5, http://publica.fraunhofer.de/documents/N-484817.html, 2017.

Dörenkämper, M., Olsen, B. T., Witha, B., Hahmann, A. N., Davis, N. N., Barcons, J., Ezber, Y., García-Bustamante, E., González-Rouco, J. F., Navarro, J., Sastre-Marugán, M., Sīle, T., Trei, W., Žagar, M., Badger, J., Gottschall, J., Sanz Rodrigo, J., and Mann, J.: The Making of the New European Wind Atlas – Part 2: Production and Evaluation, Geosci. Model Dev. Discuss., 2020, 1–37, https://doi.org/10.5194/gmd-2020-23, 2020.

Echeverri, P., Fricke, T., Homsy, G., and Tucker, N.: The Energy Kite - Selected Results From the Design, Development and Testing of Makani's Airborne Wind Turbines - Part 1, Technical Report, Makani Power, https://storage.googleapis.com/x-prod.appspot.com/files/Makani_TheEnergyKiteReport_Part1.pdf, last accessed: 2022-11-09, 2020.

Eijkelhof, D., Rapp, S., Fasel, U., Gaunaa, M., and Schmehl, R.: Reference Design and Simulation Framework of a Multi-Megawatt Airborne Wind Energy System, Journal of Physics: Conference Series, 1618, https://doi.org/10.1088/1742-6596/1618/3/032020, 2020.

Ellis, G. and Ferraro, G.: The Social Acceptance of Wind Energy: Where we stand and the path ahead., EUR - Scientific and Technical Research Reports, European Commission, https://doi.org/10.2789/696070, 2016.

Emeis, S.: Wind energy meteorology : atmospheric physics for wind power generation, Green Energy and Technology, Springer, Berlin Heidelberg, https://doi.org/10.1007/978-3-642-30523-8, 12.02.03; LK 01, 2013.

Faggiani, P. and Schmehl, R.: Design and Economics of a Pumping Kite Wind Park, in: Airborne Wind Energy: Advances in Technology Development and Research, edited by Schmehl, R., pp. 391–411, Springer Singapore, Singapore, https://doi.org/10.1007/978-981-10-1947-0_16, 2018.

Fagiano, L. and Milanese, M.: Airborne Wind Energy: An overview, in: 2012 American Control Conference (ACC), pp. 3132–3143, IEEE, https://doi.org/10.1109/ACC.2012.6314801, 2012.

Floors, R., Batchvarova, E., Gryning, S.-E., Hahmann, A. N., Peña, A., and Mikkelsen, T.: Atmospheric boundary layer wind profile at a flat coastal site - wind speed lidar measurements and mesoscale modeling results, Advances in Science and Research, 6, 155–159, https://doi.org/10.5194/asr-6-155-2011, 2011.

Gaertner, E., Rinker, J., Sethuraman, L., Zahle, F., Anderson, B., Barter, G. E., Abbas, N. J., Meng, F., Bortolotti, P., Skrzypinski, W., Scott, G. N., Feil, R., Bredmose, H., Dykes, K., Shields, M., Allen, C., and Viselli, A.: IEA Wind TCP Task 37: Definition of the IEA 15-Megawatt Offshore Reference Wind Turbine, Tech. rep., NREL, https://doi.org/10.2172/1603478, 2020.

Gros, S., Zanon, M., and Diehl, M.: A relaxation strategy for the optimization of airborne wind energy systems, in: Control Conference (ECC), 2013 European, pp. 1011–1016, IEEE, Zurich, Switzerland, https://doi.org/10.23919/ECC.2013.6669670, 2013.

Haas, T., Schutter, J. D., Diehl, M., and Meyers, J.: Wake characteristics of pumping mode airborne wind energy systems, Journal of Physics: Conference Series, 1256, 012 016, https://doi.org/10.1088/1742-6596/1256/1/012016, 2019.

Hahmann, A. N., Sile, T., Witha, B., Davis, N. N., Dörenkämper, M., Ezber, Y., García-Bustamante, E., González Rouco, J. F., Navarro, J., Olsen, B. T., and Söderberg, S.: The Making of the New European Wind Atlas, Part 1: Model Sensitivity, Geosci. Model Dev. Discuss., 2020, 1–33, https://doi.org/10.5194/gmd-2019-349, 2020.

Heilmann, J. and Houle, C.: Economics of Pumping Kite Generators, in: Airborne Wind Energy, edited by Ahrens, U., Diehl, M., and Schmehl, R., pp. 271–284, Springer Berlin Heidelberg, Berlin, Heidelberg, https://doi.org/10.1007/978-3-642-39965-7_15, 2013.

Hersbach, H. and Dick, D.: ERA5 reanalysis is in production, http://www.ecmwf.int/en/newsletter/147/news/era5-reanalysis-production, last accessed: 2019-10-22, 2016.

Houska, B. and Diehl, M.: Optimal control for power generating kites, in: 2007 European Control Conference (ECC), pp. 3560–3567, IEEE, https://doi.org/10.23919/ECC.2007.7068861, 2007.

HSL: HSL. A collection of Fortran codes for large scale scientific computation, http://www.hsl.rl.ac.uk/, last accessed: 2022-03-14, 2020.

Jonkman, J., Butterfield, S., Musial, W., and Scott, G.: Definition of a 5-MW Reference Wind Turbine for Offshore System Development, Tech. rep., NREL, https://doi.org/10.2172/947422, 2009.

Kruijff, M. and Ruiterkamp, R.: A Roadmap Towards Airborne Wind Energy in the Utility Sector, in: Airborne Wind Energy: Advances in Technology Development and Research, edited by Schmehl, R., pp. 643–662, Springer Singapore, Singapore, https://doi.org/10.1007/978-981-10-1947-0_26, 2018.

Leuthold, R., De Schutter, J., Malz, E., Licitra, G., Gros, S., and Diehl, M.: Operational Regions of a Multi-Kite AWE System, in: 2018 European Control Conference (ECC), pp. 52–57, Limassol, Cyprus, https://doi.org/10.23919/ECC.2018.8550199, 2018.

Licitra, G.: Identification and optimization of an airborne wind energy system, Ph.D. thesis, University of Freiburg, https://doi.org/10.6094/UNIFR/16226, 2018.

Licitra, G., Koenemann, J., Bürger, A., Williams, P., Ruiterkamp, R., and Diehl, M.: Performance assessment of a rigid wing Airborne Wind Energy pumping system, Energy, 173, 569–585, https://doi.org/10.1016/j.energy.2019.02.064, 2019.

Lloyd, S.: Least squares quantization in PCM, IEEE Transactions on Information Theory, 28, 129–137, https://doi.org/10.1109/TIT.1982.1056489, 1982.

Loyd, M. L.: Crosswind kite power (for large-scale wind power production), Journal of Energy, 4, 106–111, https://doi.org/10.2514/3.48021, 1980.

Luchsinger, R. H.: Pumping Cycle Kite Power, in: Airborne Wind Energy, edited by Ahrens, U., Diehl, M., and Schmehl, R., pp. 47–64, Springer, Berlin, Heidelberg, https://doi.org/10.1007/978-3-642-39965-7_3, 2013.

Lunney, E., Ban, M., Duic, N., and Foley, A.: A state-of-the-art review and feasibility analysis of high altitude wind power in Northern Ireland, Renewable and Sustainable Energy Reviews, 68, 899 – 911, https://doi.org/https://doi.org/10.1016/j.rser.2016.08.014, 2017.

Malz, E., Koenemann, J., Sieberling, S., and Gros, S.: A reference model for airborne wind energy systems for optimization and control, Renewable Energy, 140, 1004 – 1011, https://doi.org/10.1016/j.renene.2019.03.111, 2019.

Malz, E., Hedenus, F., Göransson, L., Verendel, V., and Gros, S.: Drag-mode airborne wind energy vs. wind turbines: An analysis of power production, variability and geography, Energy, 193, 116 765, https://doi.org/https://doi.org/10.1016/j.energy.2019.116765, 2020a.

Malz, E., Verendel, V., and Gros, S.: Computing the power profiles for an Airborne Wind Energy system based on large-scale wind data, Renewable Energy, 162, 766 – 778, https://doi.org/https://doi.org/10.1016/j.renene.2020.06.056, 2020b.

Molina-García, A., Fernández-Guillamón, A., Gómez-Lázaro, E., Honrubia-Escribano, A., and Bueso, M. C.: Vertical Wind Profile Characterization and Identification of Patterns Based on a Shape Clustering Algorithm, IEEE Access, 7, 30 890–30 904, https://doi.org/10.1109/ACCESS.2019.2902242, 2019.

Nakanishi, M. and Niino, H.: Development of an Improved Turbulence Closure Model for the Atmospheric Boundary Layer, Journal of the Meteorological Society of Japan, 87, 895–912, https://doi.org/10.2151/jmsj.87.895, 2009.

Obukhov, A. M.: Turbulence in an atmosphere with a non-uniform temperature, Boundary-Layer Meteorology, 2, 7–29, https://doi.org/10.1007/BF00718085, 1971.

offshorewind.biz: Ampyx Power Taking First Steps Towards MW-Scale Kite, Online, https://www.offshorewind.biz/2018/12/04/ampyx-power-taking-first-steps-towards-mw-scale-kite/, last accessed: 2022-03-14, 2018.

Olauson, J.: ERA5: The new champion of wind power modelling?, Renewable Energy, 126, 322–331, https://doi.org/10.1016/j.renene.2018.03.056, 2018.

Optis, M., Monahan, A., and Bosveld, F. C.: Limitations and breakdown of Monin–Obukhov similarity theory for wind profile extrapolation under stable stratification, Wind Energy, 19, 1053–1072, https://doi.org/10.1002/we.1883, 2016.

Peña, A., Gryning, S.-E., and Floors, R.: Lidar observations of marine boundary-layer winds and heights: a preliminary study, Meteorologische Zeitschrift, 24, 581–589, https://doi.org/10.1127/metz/2015/0636, 2015.

Pedregosa, F., Varoquaux, G., Gramfort, A., Michel, V., Thirion, B., Grisel, O., Blondel, M., Prettenhofer, P., Weiss, R., Dubourg, V., Vanderplas, J., Passos, A., Cournapeau, D., Brucher, M., Perrot, M., and Duchesnay, E.: Scikit-learn: Machine Learning in Python, Journal of Machine Learning Research, 12, 2825–2830, https://doi.org/10.48550/arXiv.1201.0490, 2011.

Ranneberg, M., Wölfle, D., Bormann, A., Rohde, P., Breipohl, F., and Bastigkeit, I.: Fast Power Curve and Yield Estimation of Pumping Airborne Wind Energy Systems, pp. 623–641, Springer Singapore, Singapore, https://doi.org/10.1007/978-981-10-1947-0_25, 2018.

Salvação, N. and Guedes Soares, C.: Wind resource assessment offshore the Atlantic Iberian coast with the WRF model, Energy, 145, 276 – 287, https://doi.org/https://doi.org/10.1016/j.energy.2017.12.101, 2018.

Schelbergen, M., Kalverla, P. C., Schmehl, R., and Watson, S. J.: Clustering wind profile shapes to estimate airborne wind energy production, Wind Energy Science, 5, 1097–1120, https://doi.org/10.5194/wes-5-1097-2020, 2020.

Schmehl, R., Noom, M., and van der Vlugt, R.: Traction Power Generation with Tethered Wings, in: Airborne Wind Energy, edited by Ahrens, U., Diehl, M., and Schmehl, R., chap. 2, pp. 23–45, Springer, Berlin, Heidelberg, https://doi.org/10.1007/978-3-642-39965-7_2, 2013.

Sempreviva, A. M. and Gryning, S.-E.: Humidity fluctuations in the marine boundary layer measured at a coastal site with an infrared humidity sensor, Boundary-Layer Meteorology, 77, 331–352, https://doi.org/10.1007/BF00123531, 1996.

Skamarock, W., Klemp, J., Dudhia, J., Gill, D., Barker, D., Duda, M., Huang, X., Wang, W., and Powers, J.: A description of the advanced research WRF version 3, Tech. Rep. NCAR/TN–475+STR, NCAR - National Center for Atmospheric Research, Boulder, Colorado, USA, https://doi.org/10.5065/D68S4MVH, 2008.

Skamarock, W. C., Klemp, J. B., Dudhia, J., and Gill, D. O.: Github: Weather Research and Forecasting Model, https://github.com/wrf-model/WRF/releases, last accessed: 2022-03-16.

Skamarock, W. C., Klemp, J. B., Dudhia, J., and Gill, D. O.: A Description of the Advanced Research WRF Model Version 4.3, Technical Report, UCAR, https://doi.org/10.5065/1dfh-6p97, 2021.

Sommerfeld, M., Crawford, C., Monahan, A., and Bastigkeit, I.: LiDAR-based characterization of mid-altitude wind conditions for airborne wind energy systems, Wind Energy, 22, 1101–1120, https://doi.org/https://doi.org/10.1002/we.2343, 2019a.

Sommerfeld, M., Dörenkämper, M., Steinfeld, G., and Crawford, C.: Improving mesoscale wind speed forecasts using lidar-based observation nudging for airborne wind energy systems, Wind Energy Science, 4, 563–580, https://doi.org/10.5194/wes-4-563-2019, 2019b.

Sommerfeld, M., Dörenkämper, M., De Schutter, J., and Crawford, C.: Ground-generation airborne wind energy design space exploration, Wind Energy Science Discussions, 2020, 1–34, https://doi.org/10.5194/wes-2020-123, 2020.

Stull, R.: An Introduction to Boundary Layer Meteorology, Atmospheric and Oceanographic Sciences Library, Springer Netherlands, https://doi.org/10.1007/978-94-009-3027-8, 1988.

van der Vlugt, R., Bley, A., Noom, M., and Schmehl, R.: Quasi-steady model of a pumping kite power system, Renewable Energy, 131, 83 – 99, https://doi.org/10.1016/j.renene.2018.07.023, 2019.

Waechter, A. and Laird, C.: Ipopt (Interior Point OPTimizer), https://github.com/coin-or/Ipopt, last accessed: 2022-03-14, 2016.

Witha, B., Hahmann, A., S̄ile, T., Dörenkämper, M., Ezber, Y., García-Bustamante, E., González-Rouco, J. F., Leroy, G., and Navarro, J.: WRF model sensitivity studies and specifications for the NEWA mesoscale wind atlas production runs, Technical report, 73 pages, The NEWA consortium, 2019.

Appendix A: Figures

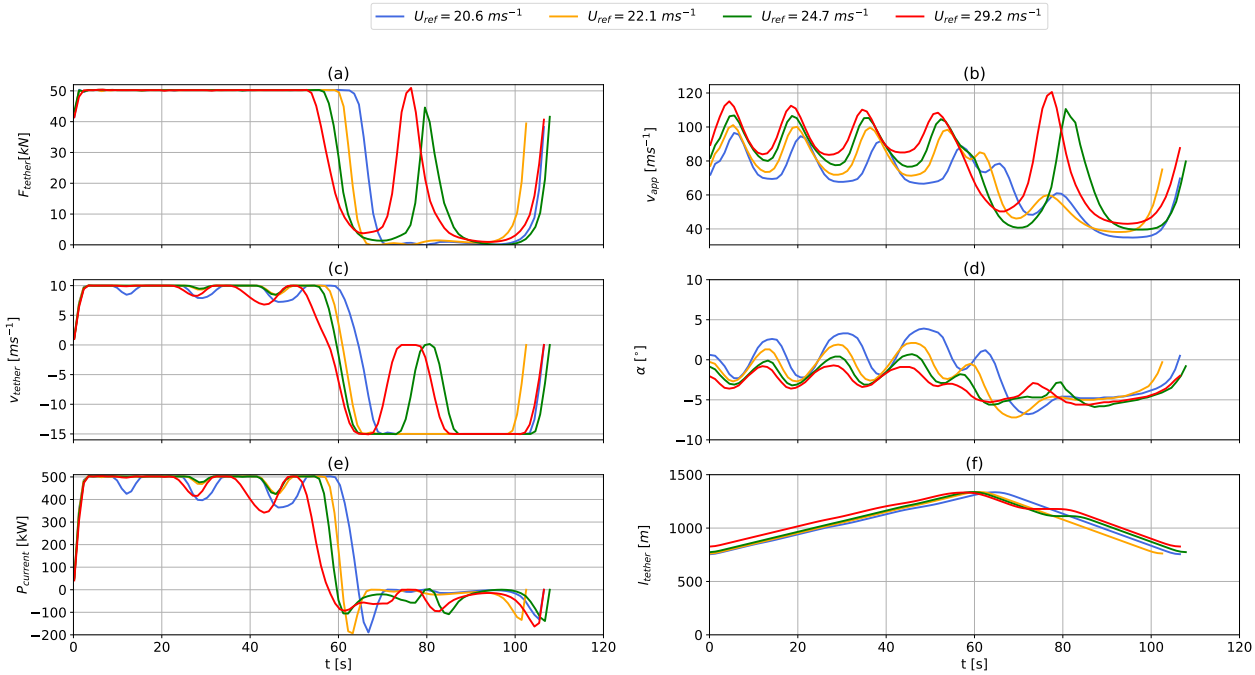

Figure A1. ~~Vertical offshore~~ Time series of instantaneous tether tension (a), apparent wind speed ~~profiles categorized into k = 10 clustered using the k-means clustering algorithm. Later analyses use k = 20 clusters. The average profile~~ (~~centroid~~b)~~is shown in blue and the profiles associated with this cluster are shown in gray. Clusters 1 to 10~~ , tether-reeling speed (~~a~~ jc)~~are sorted and labeled in ascending order~~ , angle of ~~average centroid~~ attack (d), power output (e) and tether length (f) over one pumping based on high wind speed ~~between 100 m and 400 m~~offshore WRF-simulated wind data. The ~~corresponding cluster frequency f for each cluster C is~~ results correspond to the trajectories shown in Figure ~~6~~A2. ~~The red lines mark the wind speed profile with the 5th, 50th and 95th percentile of average wind between 100 and 400 m within each cluster.~~

~~Exemplary offshore trajectories. Wind data are based on sampled WRF-simulated clusters (Section 2). Wind speed magnitude (a), and hodograph (top view) of wind velocity up to 1000 m (c). The highlighted sections indicate operating wind conditions. Panel (b) and panel (d) shows the side and top view of the corresponding awebox-optimized trajectories. The reference wind speed in the legend is $U_{\text{ref}} = \overline{U}(100\text{ m} \leq z_{\text{ref}} \leq 400\text{ m})$. The results correspond to the time series shown in Figure 17.~~

~~Time series of instantaneous tether tension (a), apparent wind speed (b), tether-reeling speed (c), angle of attack α (d), power (e) and tether length (f). The results correspond to the trajectories, based on sampled offshore WRF-simulated wind data, shown in Figure 14.~~

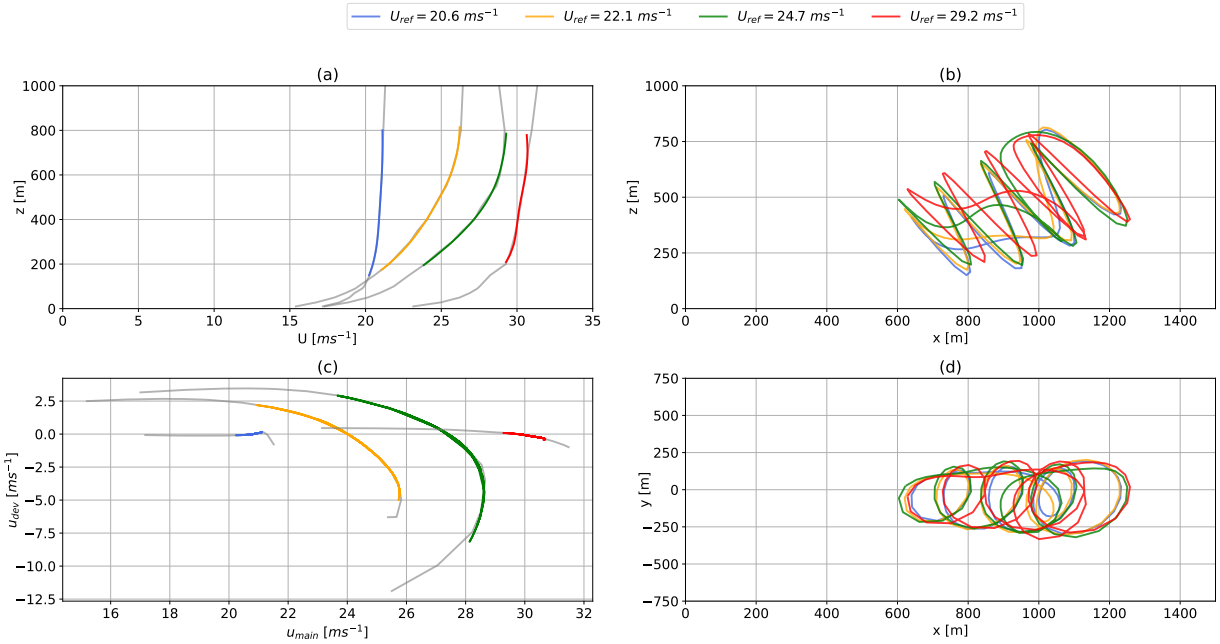

Figure A2. ~~Exemplary~~ High speed WRF-simulated vertical offshore ~~high~~ wind speed ~~trajectories. Wind data are based on sampled WRF-simulated clusters~~ profiles (~~Section 2). Wind speed magnitude~~ (a), and hodograph (top view) ~~of wind velocity~~ up to 1000 m (c). The highlighted sections indicate ~~operating~~ Lagrangian polynomial fit of the wind ~~conditions~~velocity at operating height. Panel (b) and panel (d) ~~shows~~ show the side and top view of the corresponding awebox-optimized trajectories. The reference wind speed in the legend is ~~$U_{\text{ref}} = \overline{U}(100\text{ m} \leq z_{\text{ref}} \leq 400\text{ m})$~~$\overline{U}_{\text{ref}} = \overline{U}(100\text{ m} \leq z_{\text{ref}} \leq 400\text{ m})$. The results correspond to the time series shown in Figure A1.